A displacement-based finite element formulation for general polyhedra using harmonic shape functions

J. E. Bishop[*],[†]

Computational Structural Mechanics Department, Engineering Sciences Center,
Sandia National Laboratories, Albuquerque, NM 87185–0372, USA

SUMMARY

A displacement-based continuous-Galerkin finite element formulation for general polyhedra is presented for applications in nonlinear solid mechanics. The polyhedra can have an arbitrary number of vertices or faces. The faces of the polyhedra can have an arbitrary number of edges and can be nonplanar. The polyhedra can be nonconvex with only the mild restriction of star convexity with respect to the vertex-averaged centroid. Conforming shape functions are constructed using harmonic functions defined on the undeformed configuration, thus requiring the use of a total-Lagrangian finite element formulation in large deformation applications. For nonlinear applications with computationally intensive constitutive models, it is important to minimize the number of element quadrature points. For this reason, an integration scheme is adopted in which the number of quadrature points is equal to the number of vertices. As a first step toward verifying the element behavior in the general nonlinear setting, several linear verification examples are presented using both random Voronoi meshes and distorted hexahedral meshes. For the hexahedral meshes, results for the polyhedral formulation are compared to those of the standard trilinear hexahedral formulation. The element behavior in the nearly incompressible regime is also examined. Copyright © 2013 John Wiley & Sons, Ltd.

1. INTRODUCTION

Standard finite element shapes include hexahedra (eight vertices and six faces) and tetrahedra (four vertices and four faces). The standard trilinear hexahedron can be degenerated into element shapes with fewer vertices such as the pentahedron (six vertices and five faces). While this small library of element shapes is sufficient for many applications, there is a growing need to have access to more general polyhedral shapes, ones that can have an arbitrary number of vertices and faces and can be nonconvex. It is envisioned that this larger library of element shapes will enable a rapid design-to-analysis paradigm. For example, Rashid and Selimotic [1] have proposed using a cut-cell approach for rapid meshing of geometrically complex structures. In this approach, a simple structured hexahedral mesh that overlays the domain of interest is constructed first. Intersection operations are then performed at the domain boundary, resulting in hexahedral elements in the interior of the domain and polyhedral elements on the boundary. This technique is common in computational fluid dynamics [2]. Recently, Bishop [3, 4] has advocated a method for modeling fracture processes, including fluid pressure-induced fracture propagation, based on random close-packed Voronoi meshes. In this numerical approach, fractures are allowed to nucleate and propagate only along the edges (2D)

---

*Correspondence to: J. E. Bishop, Sandia National Laboratories, P.O. Box 5800, Mail Stop 0372, Albuquerque, NM 87185–0372, USA.
[†]E-mail: jebisho@sandia.gov

and faces (3D) of the Voronoi mesh with a cohesive model used at the new fracture surfaces. Each cell of the Voronoi mesh is a polygon (2D) or polyhedron (3D) with a variable number of vertices and faces. Each polygonal or polyhedral cell is formulated as a finite element. Applications to engineered structures include the modeling of pervasive-fracture processes due to impact and blast effects. Applications to natural structures include hydraulic fracturing and the assessment of caprock integrity for geologic storage of CO_2. Only 2D results have been presented to date [3, 4]. The goal of this paper is to present recent research into a general 3D polyhedral displacement-based conforming finite element for use in nonlinear solid mechanics. This is a first step in extending the proposed fracture approach to 3D and providing increased flexibility in modeling geometrically complex structures, both engineered and natural.

Only recently have polyhedral finite element formulations been proposed in the literature [1,5–8], primarily because of the difficulty in defining shape functions, or more generally barycentric coordinates. Additionally, efficient integration of the weak form of the governing equation is challenging on a general polyhedral shape. In his seminal work, Wachspress [9] developed rational shape functions for convex polygons, but this work was not extended to convex polyhedra until 1996 [10], albeit only to polyhedra with triangular faces. There are now several new types of barycentric coordinates on polyhedra including mean-value coordinates, positive mean-value coordinates, harmonic coordinates, and several variations of maximum-entropy coordinates. An overview and comparison of these barycentric coordinates are given by Hormann and Sukumar [11]. Wicke *et al*. [6] used mean-value coordinates to develop a finite element formulation for convex polyhedra with triangular faces. An integration rule was created by placing quadrature points on the line segments joining the element centroid and each vertex, as well as the line segments joining the element centroid and each face centroid. The quadrature weights were assigned by using a partition of the element into volumes associated with quadrature points. Thus, the quadrature weights are guaranteed to be positive, and the number of quadrature points is equal to the number of vertices plus the number of faces. The element was used in simulations involving elasticity, but a convergence study was not presented. Shape functions derived from meshless methods have also been used to develop polyhedral finite elements [3, 5, 8]. Bishop [3] used the reproducing kernel method to develop shape functions for polygonal finite elements. Idelsohn *et al*. [5] developed a finite element formulation of convex polyhedra with planar faces using non-Sibsonian coordinates, which require a certain Voronoi construction within a finite element. Element integration was performed by first subdividing the polyhedron into tetrahedra. The tetrahedral subdivision was constructed by using the face centroids and the centroid of the polyhedron. Standard integration rules for tetrahedra (see, e.g., Jinyun [12]) were then used. Convergence studies were performed for the Poisson equation. Milbradt and Pick [8] developed a finite element formulation for both convex and nonconvex polyhedra with planar faces. The shape functions were constructed using natural-element coordinates, which again require a Voronoi construction within a finite element. Element integration was also developed using a tetrahedral subdivision. Convergence studies were performed for the Poisson equation. Ghosh [13] has developed extensively the Voronoi-Cell Finite Element Method based on a stress-based finite element approach. A displacement-based finite element formulation for polyhedra with planar faces, applicable to nonlinear solid mechanics, has been achieved by Rashid and Selimotic [1]. Shape functions were constructed by using a polynomial basis optimized for smoothness, while satisfying other constraints necessary for mesh convergence. The shape functions, however, are only compatible in the mean at the element faces. Rashid used an integration scheme in which a quadrature point was associated with each vertex, so that the number of quadrature points was equal to the number of vertices. The polyhedron was first partitioned into 'tributary' regions associated with each vertex. A quadrature point was placed at the centroid of each tributary region with the quadrature weight equal to the volume of the tributary region. Thus, the quadrature weights are guaranteed to be positive. Rashid performed convergence studies and provided comparisons with standard hexahedral finite element formulations for problems in elastoplasticity. Recently, Rashid and Sadri [14] have proposed a polygonal finite element formulation for use in solid mechanics in which the discrete values of both the shape functions and their derivatives at the quadrature points are determined based only on the satisfaction of linear consistency, integration consistency, and a combined smoothness and compatibility measure.

A harmonic function ψ is a solution of Laplace's equation, $\nabla^2 \psi = 0$. Harmonic coordinates on a polyhedron are developed by prescribing appropriate boundary conditions on the faces and are typically constructed hierarchically [15]. Harmonic coordinates are smooth and non-negative, at least for the exact solution of Laplace's equation. The downside to the use of harmonic coordinates is the need to solve, if only approximately, a PDE. Martin *et al.* [7] used harmonic coordinates to formulate a nonconvex polyhedral finite element with *planar* faces. A type of boundary-element method was used to solve Laplace's equation on the polyhedron. Element integration was performed by using a computationally intensive bounding-box subdivision. Convergence studies were performed for the Poisson equation, and the element was used in simulations involving elasticity. In this paper, a continuous-Galerkin finite element formulation applicable to nonlinear solid mechanics is presented for polyhedra with *nonplanar* faces. Harmonic coordinates are used to define the shape functions. The finite element method is used to approximate the harmonic functions within an element using the tetrahedral subdivision of Idelsohn *et al.* [5]. The polyhedral finite element can be nonconvex with only the mild restriction of star convexity with respect to the vertex-averaged centroid. Computational nonlinear solid mechanics typically involves the use of expensive constitutive models that are evaluated at each quadrature point within an element. Therefore, it is imperative to minimize the number of quadrature points, while avoiding the use of integration schemes that result in zero energy modes. Integration through the use of bounding-box subdivision or tetrahedral integration rules would result in a large number of quadrature points, even if only a linear integration rule was adopted (one quadrature point per tetrahedron). For this reason, the integration method of Rashid and Selimotic [1] is adopted in which the number of quadrature points is equal to the number of element vertices. This integration scheme has only linear precision (can integrate linear functions exactly), which can be problematic in passing the patch test, a test for polynomial completeness [16, Ch. 8.3]. Rashid and Selimotic [1] circumvented this problem by constraining the shape functions during their construction to satisfy a necessary integration-consistency constraint, a discrete version of the divergence theorem detailed by Krongauz and Belytschko [17] and Chen *et al.* [18]. For the present formulation, the derivatives of the shape functions are modified slightly to satisfy the discrete divergence theorem while maintaining other necessary consistency properties. These modified derivatives are called 'consistent pseudo-derivatives' by Krongauz and Belytschko [17]. The harmonic shape functions are formed directly on the initial undeformed configuration of the element, thus requiring the use of a total-Lagrangian formulation for large-deformation problems. The harmonic functions are only constructed once, at the beginning of a simulation. A mean-dilation formulation is adopted for nearly incompressible material behavior.

The polyhedral-element formulation presented here can be used in the same mesh with the standard trilinear hexahedron (if connected to quadrilateral faces on the polyhedral element), even with nonplanar faces. However, the shape functions between the two elements are not continuous, even though the patch test is satisfied [19]. If desired, the polyhedral element formulation presented here could be modified slightly to use the bilinear mapping on quadrilateral faces to ensure continuity between the two element types. This is not explored here. During the writing of this article, the author became aware of recent research by Key [20] into a mean-quadrature polyhedral finite element. The assumed structure of the polyhedron described in Section 3 is the same as that used by Key [20].

The construction of convergent PDE discretizations on general grids, including general polyhedra, has been the theme of the Mimetic Finite Difference Method (see, e.g., [21–23]). The recent Virtual Element Method [24, 25] has traits of both mimetic and finite element methods and offers a path forward for generating entirely new classes of finite element formulations on polyhedra. More analysis is needed to put the present research in context with the Virtual Element Method.

This paper is organized as follows. The total-Lagrangian form of the conservation of linear momentum is given in Section 2. The assumed structure of a polyhedron and the definition of star convexity are given in Section 3. Details of the construction of the harmonic shape functions are given in Section 4. Element integration is discussed in Section 5. The derivative corrections necessary to pass the patch test are discussed in Section 6. Convergence verification tests are presented in Section 7. While the presented finite element formulation is intended for nonlinear applications, only linear elastic examples are presented as a first step toward the more general goal. Numerical

convergence studies are performed using both Voronoi meshes and distorted hexahedral meshes. Comparisons to the trilinear hexahedron are given. Behavior near the incompressible limit is also studied. Finally, summary and conclusions are given in Section 8.

2. TOTAL-LAGRANGIAN FORMULATION

Consider the motion of a body $\mathcal{B}$ with interior domain Ω and boundary Γ subjected to a body force **b** and applied tractions **t**. A Lagrangian description of the motion of $\mathcal{B}$ is used. The initial configuration of the body is denoted by Ω_o with boundary Γ_o. In the initial configuration, the position vector of a material point is denoted by **X**. In the deformed configuration, the position of a material point is denoted by **x**. The displacement vector **u** is given by $\mathbf{u} = \mathbf{x} - \mathbf{X}$. The harmonic shape functions described in Section 4 will be constructed directly on the initial configuration as well as the integration scheme. Therefore, a *total*-Lagrangian formulation of the governing equations is appropriate. The conservation of linear momentum is given by [16, Ch. 4.7]

$$\frac{\partial \mathbf{P}}{\partial \mathbf{X}} : \mathbf{I} + \rho_o \mathbf{b} = \rho_o \ddot{\mathbf{u}} \tag{1}$$

with boundary conditions

$$\mathbf{u} = \bar{\mathbf{u}} \quad \text{on} \quad \Gamma_u \quad \text{and} \quad \mathbf{P} \cdot \mathbf{N} = \mathbf{t}_o \quad \text{on} \quad \Gamma_t \tag{2}$$

where **P** is the first Piola–Kirchhoff stress tensor, **I** is the identity tensor, ρ_o is the initial density, **b** is the body force vector per unit mass, $\ddot{\mathbf{u}}$ is the acceleration vector, **N** is the outward unit normal on Γ_o, $\mathbf{t}_o$ is the traction vector per unit initial area, and $\overline{\Gamma_u \cup \Gamma_t} = \Gamma_o$ and $\Gamma_u \cap \Gamma_t = \emptyset$.

The weak form of Equations (1) and (2) is given by the following variational problem [16, Ch. 4.8]. Find $\mathbf{u} \in H^1$ with $\mathbf{u} = \bar{\mathbf{u}}$ on Γ_u such that

$$\int_{\Gamma_t} \mathbf{t}_o \cdot \delta\mathbf{u} \, d\Gamma_o + \int_{\Omega_o} \rho_o \mathbf{b} \cdot \delta\mathbf{u} \, d\Omega_o - \int_{\Omega_o} \mathbf{P} : (\partial(\delta\mathbf{u})/\partial\mathbf{X}) \, d\Omega_o - \int_{\Omega_o} \rho_o \ddot{\mathbf{u}} \cdot \delta\mathbf{u} \, d\Omega_o = 0 \tag{3}$$

for all *test* functions $\delta\mathbf{u} \in H_o^1$. Here, H^1 is the Sobolev function space of degree one containing functions that possess square-integrable weak derivatives, and $H_o^1 = \{\mathbf{u} \in H^1 \mid \mathbf{u} = 0 \text{ on } \Gamma_u\}$. Any $u \in H^1$ is referred to as a *trial* function. The Bubnov–Galerkin procedure for obtaining an approximate solution to Equation (3) uses a finite dimensional approximation to H^1, denoted by V^h, with $V^h \subset H^1$ and $V_o^h = \{\mathbf{u}^h \in V^h \mid \mathbf{u}^h = 0 \text{ on } \Gamma_u\}$. Let $\{\phi_I, I = 1, \ldots, N\}$ be a basis for V^h so that any $\mathbf{u}^h \in V^h$ may be written as $\mathbf{u}^h(\mathbf{X}) = \sum_{I=1}^{N} \mathbf{u}_I \phi_I(\mathbf{X})$. A finite element approximation entails choosing basis functions with local support defined by a mesh. Let Ω_e represent the domain of a finite element with vertex (nodal) coordinates $\{\mathbf{X}^a, a = 1, \ldots, N_v\}$. The structure of each polyhedral element will be described in Section 3. The basis functions $\phi_I(\mathbf{X})$ may be decomposed into element shape functions denoted as $\{\psi^a(\mathbf{X}), a = 1, \ldots, N_v\}$, where N_v is the number of vertices in a polyhedron. The construction of the element shape functions will be described in Section 4. The integration scheme for approximating the integrals in Equation (3) will be described in Section 5.

3. STRUCTURE OF A POLYHEDRAL ELEMENT

A polyhedron, as defined here, is a simply connected domain with an orientable surface. The surface is partitioned into faces. Each face is simply connected and bounded by a circuit of edges. Each edge is a line segment connecting two vertices and only two faces. With this definition, the Euler characteristic is 2 so that $N_v - N_e + N_f = 2$, where N_e is the number of edges and N_f is the number of faces [26, p.12]. This identity is useful for detecting invalid polyhedral definitions.

A star-convex domain is a domain in which there exists a point in the interior that can 'see' the domain boundary without obstruction. That is, there exists a point in the domain such that a line segment connecting this point and any point on the domain boundary does not intersect the boundary at additional points. A domain is star convex with respect to a specific point if a line segment connecting this point and any point on the domain boundary does not intersect the boundary at
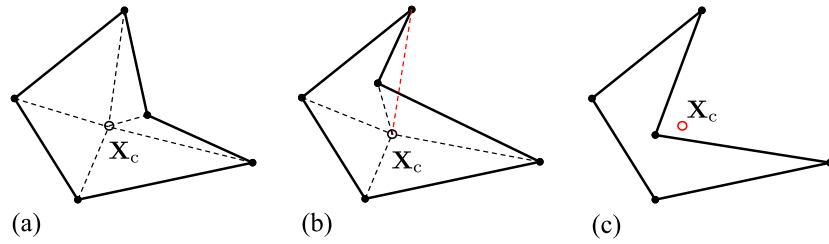
(a) (b) (c)

Figure 1. Example polygons and their vertex-averaged centroid $\mathbf{X}_c$: (a) a polygon that is star convex with respect to $\mathbf{X}_c$, (b) a polygon that is *not* star convex with respect to $\mathbf{X}_c$, and (c) a polygon in which $\mathbf{X}_c$ is not in the interior of the polygon. Example (a) is a valid element shape. Examples (b) and (c) are invalid.

additional points. Any domain that is star convex with respect to a specific point is thus star convex. This concept is illustrated in Figure 1. For convenience in the construction of the harmonic shape functions described in Section 4, as well as the finite element integration scheme described in Section 5, a polyhedron is assumed to be star convex with respect to the vertex-averaged centroid $\mathbf{X}_c$ defined as

$$\mathbf{X}_c \doteq \frac{1}{N_v} \sum_{a=1}^{N_v} \mathbf{X}^a .$$ (4)

This requirement precludes $\mathbf{X}_c$ from being exterior to the polyhedron as shown in Figure 1(c). A polyhedral formulation without this shape restriction could be obtained at the expense of a more sophisticated subdivision than adopted in Section 4.

The classic definition of a polyhedron assumes planar faces. Here, this definition is generalized to nonplanar faces. A given face is specified by its circuit of vertices $\{\mathbf{X}^a, a = 1, \ldots, N_{fv}\}$. As noted previously, each edge on the face is a line segment joining two face vertices $\{\mathbf{X}^a, \mathbf{X}^{a+1}\}$. Given this circuit of edges on a face, the explicit geometry of the face is not uniquely defined. Here, the face geometry is fully specified by using the vertex-averaged center of the face $\mathbf{X}_{fc}$ defined as

$$\mathbf{X}_{fc} \doteq \frac{1}{N_{fv}} \sum_{a=1}^{N_{fv}} \mathbf{X}^a .$$ (5)

Each face is uniquely defined by connecting the face vertex with $\mathbf{X}_{fc}$ to form a set of subdivision triangles as shown in Figure 2. This geometric construction of a face is computationally simple and convenient but also serves two other purposes. (1) The face now represents a barycentric mapping, which is a necessary property in the construction of the element shape functions as described in
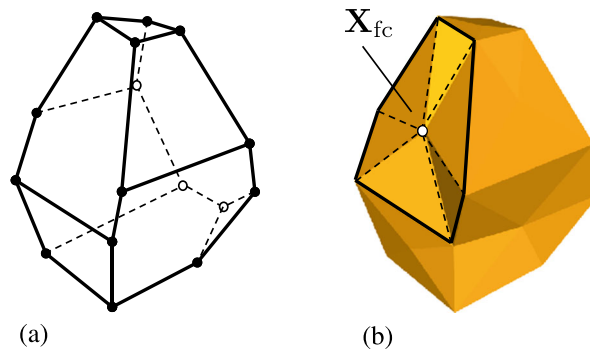

(a) (b)

Figure 2. (a) An example polyhedron consisting of 16 vertices, 10 faces, and 24 edges. The faces are non-planar and therefore not uniquely defined by the face vertices and edges alone. (b) Each face is uniquely defined by subdivision triangles connecting the face vertices and the vertex-averaged face centroid $\mathbf{X}_{fc}$.

Section 4. (2) The special case of a quadrilateral face is weakly compatible but not continuous, with the face of the trilinear hexahedron as discussed by Dohrmann and Key [19]. This latter purpose is useful in transitioning from a polyhedral mesh to a hexahedral mesh. More general face constructions are possible. For example, using a bilinear mapping for a quadrilateral would result in a continuous shape function when paired with a trilinear hexahedron.

4. HARMONIC SHAPE FUNCTIONS

Before introducing harmonic shape functions on general polyhedra, the shape functions for the trilinear hexahedron are briefly reviewed, and their essential properties enumerated. It will be shown that the harmonic shape functions posses these properties as well.

4.1. Trilinear shape functions on hexahedra

The shape functions of the trilinear hexahedron are defined using a 'parent' parametric space $\boldsymbol{\xi} \doteq (\xi, \eta, \zeta)$ as shown in Figure 3. The element shape functions $\{\psi^a(\boldsymbol{\xi}), a = 1, \ldots, 8\}$ are given by [27, Ch. 3.5]

$$\psi^a = \frac{1}{8}(1 \pm \xi)(1 \pm \eta)(1 \pm \zeta) \tag{6}$$

where $(\xi, \eta, \zeta) \in [-1, 1] \times [-1, 1] \times [-1, 1] \doteq \Omega_\square$. The vertex (node) coordinates are $\boldsymbol{\xi}^a \doteq (\pm 1, \pm 1, \pm 1)$ with appropriate signs for each $a = 1, \ldots, 8$ inferred from Figure 3(a). These shape functions have several desirable properties:

(i) The shape functions form a partition of unity,

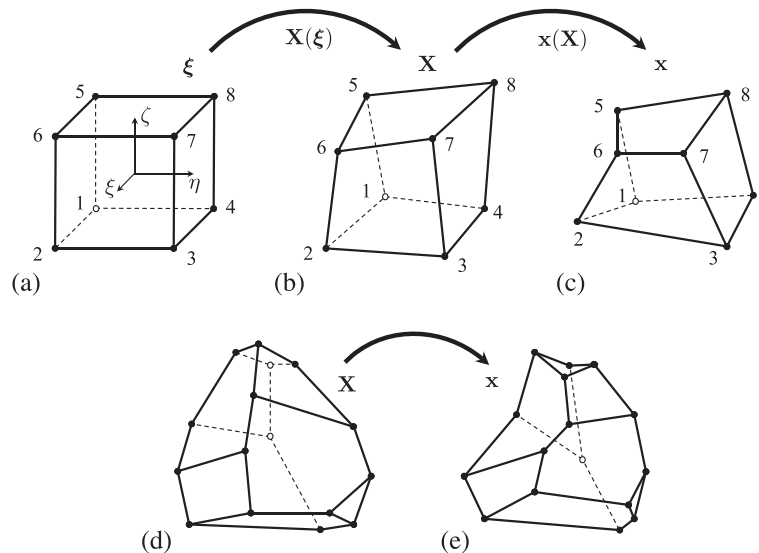$$\sum_{a=1}^{8} \psi^a(\boldsymbol{\xi}) = 1, \quad \boldsymbol{\xi} \in \Omega_\square. \tag{7}$$

Figure 3. (a)–(c) The shape functions of the trilinear hexahedron are defined on the parametric space $\boldsymbol{\xi}$. A deformed hexahedron in the original configuration $\mathbf{X}$ is obtained from the mapping $\mathbf{X}(\boldsymbol{\xi})$ from parametric space to the original configuration. A deformed hexahedron in the current configuration $\mathbf{x}$ is obtained from the mapping $\mathbf{x}(\mathbf{X}(\boldsymbol{\xi}))$ from parametric space to the current configuration. (d)–(e) In contrast, the shape functions in the polyhedral formulation are defined directly on the original configuration $\mathbf{X}$ so that the deformed polyhedron is a function only of the original configuration $\mathbf{x}(\mathbf{X})$.

(ii) The shape functions reproduce linear fields,

$$\sum_{a=1}^{8} \psi^a(\boldsymbol{\xi})\, \boldsymbol{\xi}^a = \boldsymbol{\xi}\,, \quad \boldsymbol{\xi} \in \Omega_\square. \tag{8}$$

(iii) The shape functions possess the Kronecker-delta property at the vertices,

$$\psi^a(\boldsymbol{\xi}^b) = \delta_{ab}\,, \tag{9}$$

where $\delta_{ab} = 1$ if $a = b$ and zero otherwise.

(iv) The shape functions are non-negative,

$$\psi^a(\boldsymbol{\xi}) \geqslant 0\,, \quad \boldsymbol{\xi} \in \Omega_\square\,. \tag{10}$$

Properties 1 and 2 are key properties and are collectively referred to as linear consistency. The first three properties classify the shape functions more generally as barycentric coordinates [11]. Property 3 enables the shape functions to be used as basis functions for barycentric interpolation of vertex data f^a by

$$f(\boldsymbol{\xi}) \doteq \sum_{a=1}^{8} \psi^a(\boldsymbol{\xi})\, f^a\,. \tag{11}$$

Properties 1 and 2 guarantee that this interpolation function reproduces affine functions (a linear transformation followed by a translation). That is, if the vertex data f^a in Equation (11) are given an affine transformation, then the new interpolation function is equivalent to the affine transformation applied directly to $f(\boldsymbol{\xi})$. For solid mechanics, affine transformations are equivalent to rigid body motions and constant strain states. This invariance under affine transformations is a necessary condition for convergence of the finite element method [16, Ch. 8.2.2; 27, Ch. 3.1; 28]. Properties 1 and 4 give that Equations (8) and (11) are convex combinations, so that the value of the interpolation function lies within the convex hull of the vertex data.

The position vectors within a finite element in both initial and current configurations are defined through the use of Equation (11),

$$\mathbf{X} \doteq \sum_{a=1}^{8} \psi^a(\boldsymbol{\xi})\, \mathbf{X}^a \quad \text{and} \quad \mathbf{x} \doteq \sum_{a=1}^{8} \psi^a(\boldsymbol{\xi})\, \mathbf{x}^a\,. \tag{12}$$

The displacement field is then given by

$$\mathbf{u} = \mathbf{x} - \mathbf{X} = \sum_{a=1}^{8} \psi^a(\boldsymbol{\xi})\, \mathbf{u}^a\,. \tag{13}$$

This is an isoparametric mapping because both the spatial coordinate $\mathbf{x}$ and the displacement field $\mathbf{u}$ use the same mapping functions [27, Ch. 3.3]. Finally, note that the shape functions on each face of the hexahedron depend only upon the four vertices of that face. Thus, two elements that share the same face will have continuous shape functions.

4.2. Harmonic functions on general polyhedra

Unlike the trilinear hexahedron, which has an explicit functional form for the shape functions, the shape functions for a polyhedron are defined implicitly using harmonic functions. A harmonic function ψ is a solution of Laplace's equation,
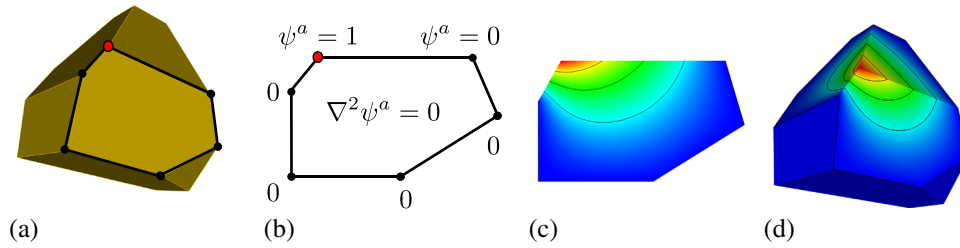
$$\nabla^2 \psi = 0\,. \tag{14}$$

Figure 4. For a polyhedron with *planar* faces, the harmonic shape functions can be obtained hierarchically [15]. (a–c) For a given vertex a (red circle), the harmonic shape function ψ^a is obtained by first solving $\nabla^2 \psi^a = 0$ each edge with end conditions of 0 or 1. These are simply linear functions. These edge solutions then become boundary conditions for solving $\nabla^2 \psi^a = 0$ on each face. (d) These face solutions then become boundary conditions for solving $\nabla^2 \psi^a = 0$ in the interior of the polyhedron.

This partial differential equation is solved, with appropriate boundary conditions, directly on the polyhedral element domain in the initial configuration with coordinates $\mathbf{X}$. There is no mapping to a parent or parametric coordinate system $\boldsymbol{\xi}$ as with the hexahedral element (Figure 3). For a given vertex a, with appropriate boundary conditions, a unique harmonic shape function $\psi^a(\mathbf{X})$ exists, and the collection of shape functions for the polyhedral element forms a set of barycentric coordinates. For polyhedra with *planar* faces, Joshi *et al.* [15] prescribed a hierarchical construction of each three-dimensional shape function by first solving Equation (14) on each edge (1D) with boundary conditions of 1 if the edge end-point is vertex a or 0 if not (the solution of which is just a linear function), then using these edge solutions to provide boundary conditions for solving Equation (14) on each face (2D), and finally using these face solutions as boundary conditions for solving Equation (14) in the volume (3D). With this construction, note that ψ^a is identically zero on all faces not attached to vertex a. This procedure is illustrated in Figure 4. This procedure is repeated for each shape function. Joshi *et al.* [15] provides a proof that these shape functions form a partition of unity and reproduce linear fields. These shape functions possess the Kronecker-delta property at the vertices. Because Equation (14) is an elliptic operator and the boundary conditions are in the range $[0, 1]$, the shape functions are non-negative [29]. Furthermore, the harmonic shape functions do not possess local minima or maxima on the interior of the element [29]. In summary,

(i) The polyhedral shape functions form a partition of unity,

$$\sum_{a=1}^{N_v} \psi^a(\mathbf{X}) = 1 , \quad \mathbf{X} \in \Omega_e . \tag{15}$$

(ii) The polyhedral shape functions reproduce linear fields,

$$\sum_{a=1}^{N_v} \psi^a(\mathbf{X}) \, \mathbf{X}^a = \mathbf{X} , \quad \mathbf{X} \in \Omega_e . \tag{16}$$

(iii) The polyhedral shape functions possess the Kronecker-delta property at the vertices,

$$\psi^a(\mathbf{X}^b) = \delta_{ab} , \qquad a, b \in \{1, \dots, N_v\} . \tag{17}$$

(iv) The polyhedral shape functions are non-negative,

$$\psi^a(\mathbf{X}) \geqslant 0 , \quad \mathbf{X} \in \Omega_e , \quad a \in \{1, \dots, N_v\} . \tag{18}$$

Note that, as with the trilinear hexahedral shape functions, the shape functions on each face of a polyhedron depend only upon the vertices of that face. Thus, two polyhedral elements that share the same face will form continuous basis functions.

For *nonplanar* faces, the hierarchical shape-function construction of Joshi *et al.* [15] must be modified; otherwise, the resulting shape functions will not reproduce linear fields, Equation (16).

Consider the shape function $\psi^a(\mathbf{X})$ corresponding to vertex (node) a. Instead of constructing harmonic functions on each face, the triangular subdivision introduced in Section 3 is used on each face. The shape function values on each edge are prescribed as in the case with planar faces. The shape function values on any face not attached to vertex a are identically zero. For any face attached to vertex a, the shape function value at vertex-averaged face centroid $\mathbf{X}_{fc}$ is defined as $\psi^a(\mathbf{X}_{fc}) \doteq 1/N_{fv}$. Each vertex of the triangle subdivision is now defined as either 0, 1, or $1/N_{fv}$. The values of ψ^a on the remainder of the face are defined by linear interpolation on each triangle. This construction is shown in Figure 5. The boundary conditions of the shape function ψ^a are now fully specified. It remains only to actually solve Equation (14) on the interior of the polyhedron.

Joshi *et al.* [15] used a multigrid finite difference approach with an overlaid grid to solve Equation (14), which required special consideration for enforcement of the face boundary conditions. Martin *et al.* [7] used a boundary-element method to solve Equation (14). While a boundary-element approach is perhaps the least intrusive, here a finite element approach is used because a volume subdivision of the polyhedral element is needed for defining the element quadrature points as described in Section 5. From the assumption of star convexity with respect to the vertex-averaged centroid $\mathbf{X}_c$ (Section 3), a tetrahedral subdivision mesh can be obtained by connecting each triangle within the face subdivision to $\mathbf{X}_c$, as described by Idelsohn *et al.* [5] and shown in Figure 6. This initial subdivision will be referred to as the $r0$–subdivision. It contains $\sum_{i=1}^{N_f} N_{fv}$ tetrahedra. A hierarchical refinement of this initial subdivision tetrahedral mesh is obtained by dividing each tetrahedron into eight tetrahedra using the midpoints of each tetrahedral edge as shown in Figure 6. The first refinement is referred to as the $r1$–subdivision. The second refinement is referred to as the
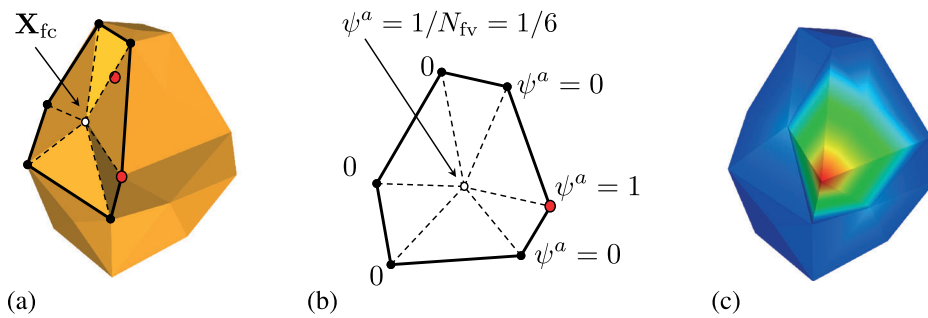

Figure 5. (a) For a polyhedron with *nonplanar* faces, the boundary conditions for each harmonic shape function ψ^a are specified directly using the triangle subdivision shown in Figure 2. (b) Vertex a is assigned a value of 1. All other vertices are assigned a value of 0. The vertex-averaged centroid $\mathbf{X}_{fc}$ of each face attached to vertex a is assigned a value of $1/N_{fv}$. All other vertex-averaged face centroids are assigned a value of 0. (c) The value of ψ^a within each face triangle is defined by linear interpolation.
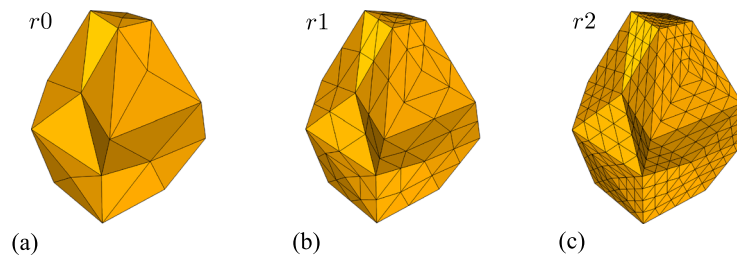

Figure 6. Values of the harmonic shape function ψ^a in the interior of the polyhedron are obtained by solving $\nabla^2 \psi^a = 0$ with boundary conditions shown in Figure 5, using the finite element method and a subdivision tetrahedral mesh. (a) This tetrahedral mesh is obtained by connecting the subdivision face triangles shown in Figure 2 with the vertex-averaged polyhedron centroid $\mathbf{X}_c$. This base tetrahedral mesh is referred to as the $r0$–subdivision. (b) A hierarchical refinement of this subdivision tetrahedral mesh is obtained by dividing each tetrahedron into eight tetrahedra. The first refinement is referred to as the $r1$–subdivision. (c) This hierarchical refinement is repeated to obtain the $r2$–subdivision.

$r2$–subdivision. The standard finite element method is then used to solve Equation (14) subjected to the face boundary conditions described previously. Note that the higher subdivisions do not change the face boundary conditions when solving Equation (14), but merely increase the accuracy in the interior of the element. For the $r0$–subdivision, there is only one unknown (at the polyhedron centroid). For the $r1$–subdivision, there are $N_v + N_f + 1$ unknowns. Because the number of unknowns is small, a direct solver is used to solve the system of equations. The question arises as to whether the finite element approximation of Equation (14) has the same properties given in Equations (15) to (18). A proof that Equations (15) to (17) still hold for the finite element approximation is given in the following theorem.

Theorem 1
Let Ω_e represent an arbitrary element with boundary Γ_e and vertex coordinates $\{\mathbf{X}^a, a = 1, \ldots, N_v\}$. The finite element approximations $\{\psi^{ah}, a = 1, \ldots, N_v\}$ to the harmonic shape functions $\{\psi^a, a = 1, \ldots, N_v\}$ possess the linear consistency properties,

$$\sum_{a=1}^{N_v} \psi^{ah}(\mathbf{X}) = 1, \quad \mathbf{X} \in \Omega_e, \tag{19}$$

$$\sum_{a=1}^{N_v} \psi^{ah}(\mathbf{X}) \mathbf{X}^a = \mathbf{X}, \quad \mathbf{X} \in \Omega_e. \tag{20}$$

Proof
For clarity in the proof, both vector and indicial notation will be intermixed. The notation $()_{,i}$ represents the derivative with respect to the coordinate direction X_i, $i = 1, 2, 3$. Repeated subscripts imply summation. The finite element solution of Equation (14) is given by the following variational problem. Find $\psi^{ah} \in V^h \subset H^1$ with $\psi^{ah} = \overline{\psi^a}$ on Γ_e such that

$$\int_{\Omega_e} \psi^{ah}_{,i} \, v_{,i} \, d\Omega_e = 0 \tag{21}$$

for all test functions $v \in V_o^h$ where $V_o^h = \{v \in V^h \mid v = 0 \text{ on } \Gamma_e\}$. By the construction process described in Section 4.2, the finite element approximations ψ^{ah} to ψ^a possess the linear consistency properties on the boundary Γ_e,

$$\sum_{a=1}^{N_v} \psi^{ah}(\mathbf{X}) = 1, \quad \mathbf{X} \in \Gamma_e, \tag{22}$$

$$\sum_{a=1}^{N_v} \psi^{ah}(\mathbf{X}) \mathbf{X}^a = \mathbf{X}, \quad \mathbf{X} \in \Gamma_e. \tag{23}$$

Summing Equation (21) from $a = 1$ to $a = N_v$ results in

$$\sum_{a=1}^{N_v} \int_{\Omega_e} \psi^{ah}_{,i} \, v_{,i} \, d\Omega_e = \int_{\Omega_e} \left(\sum_{a=1}^{N_v} \psi^{ah} \right)_{,i} v_{,i} \, d\Omega_e = 0 \quad \text{for all} \quad v \in V_o^h. \tag{24}$$

Let $\Psi \doteq \sum_{a=1}^{N_v} \psi^{ah}$. From Equation (22), note that $\Psi = 1$ on Γ_e. Thus, Ψ satisfies the following variational problem,

$$\int_{\Omega_e} \Psi_{,i} \, v_{,i} \, d\Omega_e = 0 \quad \text{for all} \quad v \in V_o^h \quad \text{with} \quad \Psi = 1 \quad \text{on} \quad \Gamma_e. \tag{25}$$

The unique solution to this problem is $\Psi = 1$. Thus, $\sum_{a=1}^{N_v} \psi^{ah} = 1$, which proves Equation (19).

Now, multiply Equation (21) by $\mathbf{X}^a$ and sum from $a = 1$ to $a = N_v$ giving

$$\sum_{a=1}^{N_v} \mathbf{X}^a \int_{\Omega_e} \psi_{;i}^{ah} \, v_{,i} \, d\Omega_e = 0 \quad \text{for all} \quad v \in V_o^h \, . \tag{26}$$

Because $\mathbf{X}^a$ is a constant, this can be written as

$$\int_{\Omega_e} \left(\sum_{a=1}^{N_v} \psi^{ah} \mathbf{X}^a \right)_{,i} v_{,i} \, d\Omega_e = 0 \quad \text{for all} \quad v \in V_o^h \, . \tag{27}$$

Let $\Psi \doteq \sum_{a=1}^{N_v} \psi^{ah} \mathbf{X}^a$. From Equation (23), note that $\Psi = \mathbf{X}$ on Γ_e. Thus, Ψ satisfies the following variational problem,

$$\int_{\Omega_e} \Psi_{,i} \, v_{,i} \, d\Omega_e = 0 \quad \text{for all} \quad v \in V_o^h \quad \text{with} \quad \Psi = \mathbf{X} \quad \text{on} \quad \Gamma_e \, . \tag{28}$$

The unique solution to this problem is $\Psi = \mathbf{X}$. Thus, $\sum_{a=1}^{N_v} \psi^{ah} \mathbf{X}^a = \mathbf{X}$, which proves Equation (20). $\square$

Note, however, that a finite element approximation of the harmonic shape function can result in a violation of the positivity property, Equation (18). Numerical experiments have shown any negative values to be relatively small and isolated to regions near the boundary of the polyhedron. This property is not necessary for the element formulation, however. Furthermore, results from the example problems given in Section 7 show that the more accurate solution of Equation (14) for the shape functions does not necessarily translate into a more accurate finite element solution of the solid mechanics problem, a somewhat counterintuitive result. The $r1$–subdivision appears to be optimal, although this may be problem dependent.

Note that although the shape functions are initially obtained for the entire polyhedral element, only the value at each quadrature point is actually stored, along with the shape-function derivatives. All other information is discarded as it is not needed in the finite element simulation. Table I gives the maximum absolute error in the linear-consistency properties, Equations (15) and (16), for the polyhedron shown in Figure 5. The maximum is taken over all of the quadrature points defined in Section 5. The error is on the order of machine precision. For this polyhedron, the maximum out-of-plane measure for all the faces is 10%, where the out-of-plane measure is defined as the maximum distance of all face vertices to a plane passing through $\mathbf{X}_{fc}$ with normal given by the average normal of the subdivision triangles, and 'distance' is obtained from a projection along this normal. The percentage is taken with respect to the diameter of a face, where 'diameter' is the maximum distance between pairs of face vertices.

The derivatives of the shape functions are obtained from the finite element solution by first calculating the derivative in each subdivision tetrahedron, which is constant within a tetrahedron. The derivatives at the quadrature points could be obtained directly from this piecewise constant field. However, a perturbation in the element shape could possibly result in large change in the derivative

Table I. Error in the linear-consistency properties of the polyhedral shape functions for different levels of the tetrahedral subdivision, for the polyhedral element shown in Figure 5.

Subdivision	$\displaystyle \max_{k \in \{1,\dots,N_{\text{i.p.}}\}} \left[\sum_{a=1}^{N_v} \psi^a(\mathbf{X}^k) - 1 \right]$	$\displaystyle \max_{\substack{k \in \{1,\dots,N_{\text{i.p.}}\} \\ j \in \{1,2,3\}}} \left[\sum_{a=1}^{N_v} \psi^a(\mathbf{X}^k) X_j^a - X_j^k \right]$
$r0$	3.33×10^{-16}	5.55×10^{-16}
$r1$	6.66×10^{-16}	5.55×10^{-16}
$r2$	1.55×10^{-15}	5.55×10^{-16}

Table II. Error in the linear-consistency properties of the derivatives of the polyhedral shape functions for different levels of the tetrahedral subdivision, for the polyhedral element shown in Figure 5.

Subdivision	$\displaystyle\max_{\substack{k\in\{1,\dots,N_{\text{i.p.}}\}\\i\in\{1,2,3\}}}\left[\sum_{a=1}^{N_{\text{v}}}\psi^a_{,i}(\mathbf{X}^k)\right]$	$\displaystyle\max_{\substack{k\in\{1,\dots,N_{\text{i.p.}}\}\\i,j\in\{1,2,3\}}}\left[\sum_{a=1}^{N_{\text{v}}}\psi^a_{,i}(\mathbf{X}^k)X^a_j-\delta_{ij}\right]$
$r0$	1.14×10^{-15}	2.64×10^{-16}
$r1$	2.22×10^{-15}	5.55×10^{-16}
$r2$	7.72×10^{-15}	1.64×10^{-15}

at the quadrature point (because the quadrature point might be located on an edge of the subdivision tetrahedral mesh). To avoid this, the derivatives of each attached tetrahedral element are arithmetically averaged at the nodes of the subdivision tetrahedral mesh. This results in a continuous field from which to extract the derivatives at the quadrature points by simple interpolation within a tetrahedron. Other smoothing algorithms could be explored. Recall from Section 2 that in the total-Lagrangian formulation of the governing equations, all derivatives are with respect to $\mathbf{X}$, the coordinate in the initial configuration, and all integration is performed in the initial configuration. Thus, for a total-Lagrangian formulation, this construction of the polyhedral shape functions and their derivatives is only be performed once, at the beginning of a simulation.

A necessary consistency condition on the shape-function derivatives for passing the patch test (Section 6) is obtained by taking the derivative of Equations (15) and (16) in each coordinate direction [17], resulting in

$$\sum_{a=1}^{N_{\text{v}}}\psi^a_{,i}(\mathbf{X})=0\,,\quad\sum_{a=1}^{N_{\text{v}}}\psi^a_{,i}(\mathbf{X})X^a_j=\delta_{ij}\,,\quad\mathbf{X}\in\Omega_{\text{e}}\,,\quad i,j=1,2,3\,. \tag{29}$$

Table II gives the maximum absolute error in these derivative-consistency properties for the polyhedron shown in Figure 5. The maximum is taken over all coordinate directions and over all of the quadrature points. The error is on the order of machine precision.

To avoid numerical tolerance issues, before any element processing begins, a polyhedral element is first translated to the origin and scaled so that the element diameter is 1. After constructing the element quadrature points, the shape functions, and their derivatives, all data are rescaled.

5. ELEMENT INTEGRATION

Computational nonlinear solid mechanics typically involves the use of expensive nonlinear constitutive models that are evaluated at each quadrature point within an element. Therefore, it is imperative to minimize the number of quadrature points, while avoiding the use of integration schemes that result in zero energy modes. Integration through the use of tetrahedral integration rules and the subdivision tetrahedral mesh described in Section 4.2 would result in a prohibitively large number of quadrature points. For example, the number of tetrahedra in the $r0$, $r1$, and $r2$–subdivisions of the polyhedral element shown in Figure 2 is 48, 384, and 3072, respectively, whereas the number of polyhedral vertices is only 16. For this reason, the integration method of Rashid and Selimotic [1] is adopted in which the number of quadrature points is equal to the number of element vertices. In this approach, a polyhedron is partitioned into N_{v} 'tributary' regions with each region associated with a vertex. A quadrature point is placed at the centroid of each tributary region, and the quadrature weight is simply the volume of the tributary region. Thus, the quadrature weights are guaranteed to be positive. The tributary region of vertex $\mathbf{X}^a$ is constructed by forming tetrahedra using the vertex-averaged centroid $\mathbf{X}_c$, the vertex-averaged face centroid $\mathbf{X}_{\text{fc}}$ of each face attached to $\mathbf{X}^a$, and the midpoints of each edge attached to $\mathbf{X}^a$, as shown in Figure 7. Each face connected to the vertex contributes two tetrahedra to the tributary region. This integration scheme has only linear precision (can integrate linear functions exactly), which is sufficient for convergence (see Theorem 2 in Section 6).
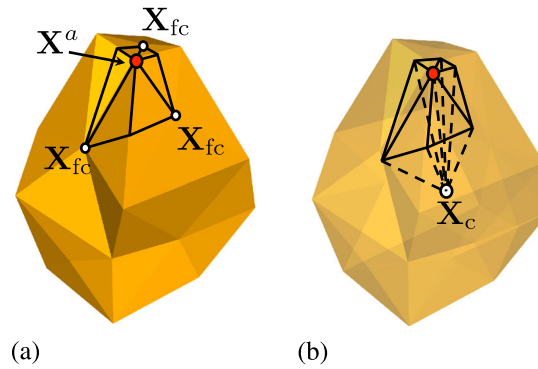
Figure 7. (a) Construction of the tributary region of a polyhedral vertex $\mathbf{X}^a$ (red circle) for use in the integration scheme of Rashid and Selimotic [1]. This region is constructed by first forming triangle facets connecting the vertex $\mathbf{X}^a$, the midpoint of each attached edge, and the vertex-averaged centroid of each attached face $\mathbf{X}_{\text{fc}}$ (cf. Figure 2). (b) These triangle facets are then joined to the vertex-averaged centroid $\mathbf{X}_{\text{c}}$ to form tetrahedra. A quadrature point is placed at the centroid of this region, and the quadrature weight is simply the volume of the tributary region.

It is tempting to use the method of moments to obtain a higher-order integration scheme (see, e.g., [30]). Numerical experiments using this approach exhibited reduced accuracy compared to the adopted first-order scheme. This result is possibly due to Runge's phenomenon [31] and the nonpolynomial nature of the shape functions, although more analysis is needed.

An integration scheme for each polyhedral face must also be defined in order to evaluate the surface traction term in Equation (3). Because the evaluation of this term does not involve the use of a constitutive model, minimizing the number of quadrature points is not critical to the overall efficiency of the element. Here, the triangular subdivision of the face described in Section 3 is used, with a three-point integration rule for second-order precision [32].

To prevent locking behavior in the nearly incompressible regime, a mean-dilation approach is used [1; 27, Ch. 4.5; 33, Ch. 4.4]. In the examples presented in Section 7, the element formulation without any correction for nearly incompressible behavior will be referred to as 'standard dilation'.

6. PATCH TEST AND DERIVATIVE CORRECTIONS

The patch test is a verification test commonly used to test new finite element formulations for polynomial completeness, that is, the ability of an arbitrary collection of elements to reproduce polynomials of a given order [16, Ch. 8.3; 27, Ch. 4.6]. The patch test consists of applying uniform tractions to the boundary of an arbitrary patch of elements, typically containing distorted elements, and then verifying that the resulting finite element solution returns the exact linear displacement field and constant strain field. Equivalently, displacement boundary conditions corresponding to the exact displacement field for a uniform stress state can be applied. The patch test is also useful in verifying the overall computer implementation, including traction and displacement boundary conditions. For the present series of patch tests, an isotropic linear elastic material model is used with Young's modulus $E = 1.0$ and Poisson's ratio $\nu = 0.3$. Tractions corresponding to a stress field with only one nonzero component with unit value are applied. This test is repeated for each of the six stress components.

The two element patches shown in Figure 8 will be used in the verification tests. Figure 8(a) is a patch of seven distorted hexahedra consisting of six elements on the boundary of the cube and one element in the interior. Figure 8(b) is a Voronoi patch of polyhedral elements, each with a different number of vertices and faces. This polyhedral mesh was created by first seeding the cube using maximal Poisson sampling, which results in a random close-packing of hard spheres [3]. A Voronoi tessellation or mesh is created by taking the dual of the Delauney triangulation of the point cloud.
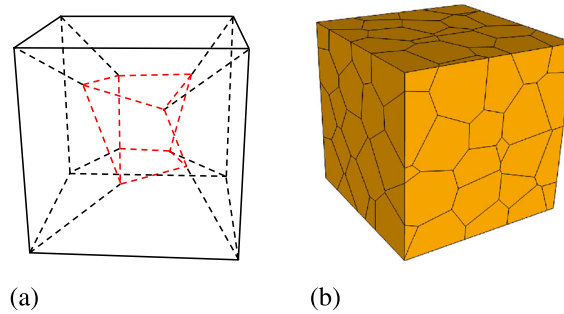
(a)	(b)

Figure 8. The two element patches used in the patch tests: (a) a cube containing seven distorted hexahedra, six elements on the boundary and one element in the interior, and (b) a random close-packed Voronoi mesh with statistics given in Figure 9.
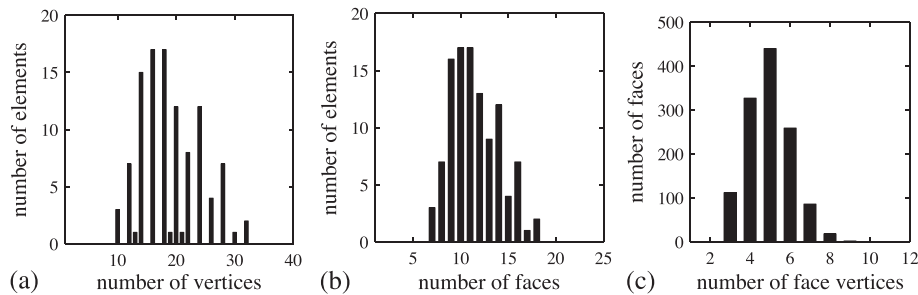

(a)	(b)	(c)

Figure 9. Histograms showing vertex and face statistics of the random close-packed Voronoi patch shown in Figure 8(b): (a) histogram of the number of elements with a given number of vertices; (b) histogram of the number of elements with a given number of faces; and (c) histogram of the number of faces with a given number of vertices.

A Voronoi mesh has strictly planar faces after its construction. However, the resulting elements typically contain a significant number of degenerate edges that need to be eliminated for numerical computations. Here, all edges with a ratio of length to element diameter less than 0.001 were eliminated by collapsing the edges to the midpoint and equivalencing nodes. The resulting minimum edge-to-diameter ratio was 0.003. This small-edge regularization warps the faces slightly. Histograms of the number of elements with a given number of vertices and faces are shown in Figure 9.

Figure 10(a) shows the result from one of the Voronoi patch tests. The patch was subjected to a uniform surface traction corresponding to a Cauchy stress field with components $\sigma_{11} = 1$ and all other components equal to zero. The $r1$–subdivision was used to form the shape functions. The deformed mesh is shown greatly exaggerated. Color represents the element-averaged stress component σ_{11}. The error in σ_{11} is over 18% and so large that it results in nonconvergence in the example problems presented in Section 7. Fundamentally, this result is due to a violation of the divergence theorem arising from the approximate numerical integration and exacerbated by the nonpolynomial nature of the shape functions. The standard finite element formulation on hexahedra does not suffer from this effect due to the polynomial basis, even though the basis is formed on the parent parametric space, a somewhat fortuitous result [28, Ch. 4.3]. Rashid and Selimotic [1] circumvented this problem by constraining the shape-function derivatives during their construction to satisfy the discrete form of the divergence theorem. In the context of meshless methods, Krongauz and Belytschko [17] first identified this integration constraint, along with the linear-consistency properties, Equation (29), as the key properties of the derivatives of the shape functions necessary for passing the patch test. The divergence theorem states that

$$\int_{\Omega_e} \psi^a_{,i}\, d\Omega = \int_{\Gamma_e} \psi^a\, n_i\, d\Gamma\,, \quad a = 1, \ldots, N_v\,, \quad i = 1, 2, 3\,, \tag{30}$$
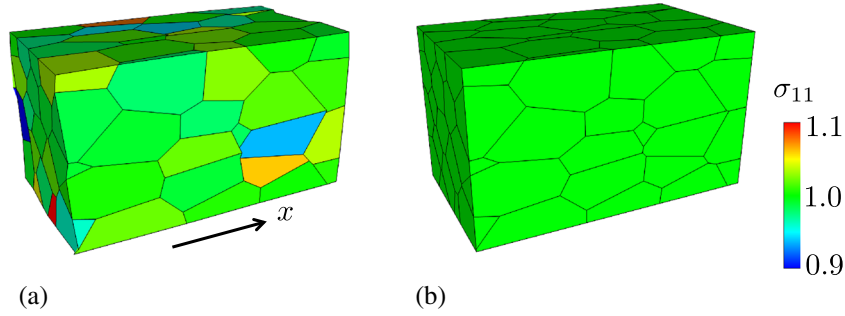
Figure 10. Results from one of the Voronoi patch tests. Color represents the element-averaged Cauchy stress component σ_{11}. The exact value is $\sigma_{11} = 1$. The deformed configuration is shown greatly exaggerated. (a) Initial result *before* correcting the derivatives of the shape functions to satisfy the integration-consistency constraint. The maximum error is 18%. (b) Result *after* correcting the derivatives to satisfy the integration-consistency constraint. The maximum error is 1.4×10^{-12}.

where n_i represents the components of the outward unit normal vector on Γ_e. In discrete form, this becomes

$$\sum_{k=1}^{N_{\text{i.p.}}} w_k \psi_{;i}^{ak} = \sum_{l=1}^{N_{\text{i.p.}}^{\Gamma}} w_l^{\Gamma} \psi^{al} n_i^l \, , \quad a = 1, \ldots, N_{\text{v}} \quad i = 1, 2, 3 \, , \tag{31}$$

where $\psi^{ak} \doteq \psi^a(\mathbf{X}^k)$ with $\mathbf{X}^k$ representing the position of a quadrature point. The quadrature weight is w_k in the element volume and w_l^{Γ} on the element surface (faces). The number of quadrature points in the element volume is $N_{\text{i.p.}}$, and the number of quadrature points on the element surface is $N_{\text{i.p.}}^{\Gamma}$. As noted by Krongauz and Belytschko [17], any violation of this integration constraint will result in incompatible strains, and thus stresses, as evidenced in Figure 10(a). Krongauz and Belytschko [17] adopted a Petrov–Galerkin approach in which the trial functions only had to satisfy Equation (29), while the test functions only had to satisfy Equation (30), in order to pass the patch test. They modified the derivatives of the trial function to satisfy Equation (29) and referred to them as 'consistent pseudo-derivatives'.

Here, a similar approach is adopted, but the Bubnov–Galerkin approach is maintained, as in the standard finite element method, so that the trial functions and test functions are the same. This results in a symmetric stiffness matrix. The derivatives of the shape functions are modified to satisfy Equation (31), while minimizing the sum of the squared differences with respect to the original values,

$$\min_{\xi^k \in \Re} \sum_{k=1}^{N_{\text{i.p.}}} \left(\xi^k - \psi_{;i}^{ak} \right)^2 \tag{32}$$

subject to the constraint

$$\sum_{k=1}^{N_{\text{i.p.}}} w_k \xi^k - \sum_{l=1}^{N_{\text{i.p.}}^{\Gamma}} w_l^{\Gamma} \psi^{al} n_i^l = 0 \, . \tag{33}$$

Let d_i^{ak} represent the solution of this constrained minimization problem. This problem is solved for each shape function $a = 1, \ldots, N_{\text{v}}$ and direction $i = 1, 2, 3$, independently, using the method of Lagrange multipliers [34, Ch. 10]. The augmented Lagrangian L_A associated with the constrained problem is defined as

$$L_A(\xi^k, \lambda) \doteq \sum_{k=1}^{N_{\text{i.p.}}} \left(\xi^k - \psi_{;i}^{ak} \right)^2 + \lambda \left(\sum_{k=1}^{N_{\text{i.p.}}} w_k \xi^k - \sum_{l=1}^{N_{\text{i.p.}}^{\Gamma}} w_l^{\Gamma} \psi^{al} n_i^l \right) , \tag{34}$$

Table III. Maximum error in the integration constraint (31) before and after the derivative-correction process, for the polyhedral element shown in Figure 5, for different levels of the tetrahedral subdivision. The maximum is taken over each coordinate direction, $i = 1, 2, 3$, and shape function, $a = 1, \ldots, N_v$.

Subdivision	Before derivative correction	After derivative correction
$r0$	0.0609	2.77×10^{-17}
$r1$	0.0138	2.77×10^{-17}
$r2$	0.0106	2.77×10^{-17}

where λ is the Lagrange multiplier. The necessary conditions for a local minimum are given by

$$\frac{\partial L_A}{\partial \xi^k} = 0, \quad k = 1, \ldots, N_{\text{i.p.}} . \tag{35}$$

This set of equations, along with the constraint Equation (33), results in a set of $N_{\text{i.p.}} + 1$ linear equations for the $N_{\text{i.p.}}$ unknowns, d_i^{ak}, and the Lagrange multiplier λ. This process is performed for each $a = 1, \ldots, N_v$ and $i = 1, 2, 3$. Note that the use of a direct solver using column storage on this system of equations is extremely efficient because all of the equations, except the constraint equation, contain only the diagonal term. Table III gives the maximum error in the integration constraint (33) before and after the derivative-correction process, for the polyhedral element shown in Figure 5, for the three subdivision levels $r0$, $r1$, and $r2$. The maximum is taken over each coordinate direction and each shape function. The error after the correction is on the order of machine precision. Typically, the changes in the derivatives are relatively small, only a few percent in the largest derivatives for the cases studied here.

Surprisingly, this procedure for modifying the shape-function derivatives does not corrupt their consistency properties given in Equation (29). A proof of this result was developed and is given in the following theorem.

Theorem 2
Let Ω_e represent an arbitrary element with volume V, boundary Γ_e, and vertex coordinates $\{\mathbf{X}^a, a = 1, \ldots, N_v\}$. Let $\{\psi^a(\mathbf{X}), a = 1, \ldots, N_v\}$ be a set of nodal shape functions with linear consistency,

$$\sum_{a=1}^{N_v} \psi^a(\mathbf{X}) = 1, \quad \mathbf{X} \in \Omega_e , \tag{36}$$

$$\sum_{a=1}^{N_v} \psi^a(\mathbf{X})\, \mathbf{X}^a = \mathbf{X}, \quad \mathbf{X} \in \Omega_e . \tag{37}$$

Let $\left\{(\mathbf{X}^k, w_k), k = 1, \ldots, N_{\text{i.p.}}\right\}$ be a set of discrete quadrature points and weights within Ω_e, with the property

$$\sum_{k=1}^{N_{\text{i.p.}}} w_k = V . \tag{38}$$

Let $\left\{\left(\mathbf{X}^l, w_l^\Gamma, \mathbf{n}^l\right), l = 1, \ldots, N_{\text{i.p.}}^\Gamma\right\}$ be a set of discrete quadrature points, weights, and outward unit normals on Γ_e, with properties (discrete divergence theorem)

$$\sum_{l=1}^{N_{\text{i.p.}}^\Gamma} w_l^\Gamma\, n_i^l = 0, \quad i = 1, 2, 3 , \tag{39}$$

$$\sum_{l=1}^{N_{\mathrm{i.p.}}^{\Gamma}} w_l^{\Gamma}\, X_j^l\, n_i^l = V \delta_{ij}\,, \quad i,j = 1,2,3\,. \tag{40}$$

The solutions d_i^{ak} of the set of constrained minimization problems

$$\min_{\xi^k \in \Re^k} \sum_{k=1}^{N_{\mathrm{i.p.}}} \left(\xi^k - \psi_{;i}^a(\mathbf{X}^k) \right)^2 \quad \text{with constraint} \quad \sum_{k=1}^{N_{\mathrm{i.p.}}} w_k\, \xi^k - \sum_{l=1}^{N_{\mathrm{i.p.}}^{\Gamma}} w_l^{\Gamma}\, \psi^a(\mathbf{X}^l)\, n_i^l = 0\,, \tag{41}$$

$a = 1,\ldots,N_{\mathrm{v}}$, $i = 1,2,3$, satisfy the consistency conditions

$$\sum_{a=1}^{N_v} d_i^{ak} = 0\,, \tag{42}$$

$$\sum_{a=1}^{N_v} d_i^{ak} X_j^a = \delta_{ij}\,, \tag{43}$$

$i,j = 1,2,3$, $k = 1,\ldots,N_{\mathrm{i.p.}}$.

Proof
For clarity in the proof, both vector and indicial notation will be intermixed. The notation $()_{,i}$ represents the derivative with respect to the coordinate direction X_i, $i = 1,2,3$. The constrained minimization problem defined by Equation (41) gives the modified derivatives of an individual shape function of an individual element at its volume quadrature points. This constrained minimization problem is solved for each shape-function derivative $\psi_{;i}^a$, $a = 1,\ldots,N_v$ and for each coordinate direction $i = 1,2,3$, independently, using the method of Lagrange multipliers [34, Ch. 10]. The augmented Lagrangian L_A associated with each constrained minimization problem is given by

$$L_A\left(\xi^k, \lambda_i^a\right) := \sum_{k=1}^{N_{\mathrm{i.p.}}} \left(\xi^k - \psi_{;i}^a(\mathbf{X}^k) \right)^2 + \lambda_i^a \left(\sum_{k=1}^{N_{\mathrm{i.p.}}} w_k\, \xi^k - \sum_{l=1}^{N_{\mathrm{i.p.}}^{\Gamma}} w_l^{\Gamma}\, \psi^a(\mathbf{X}^l)\, n_i^l \right) \tag{44}$$

where λ_i^a is the Lagrange multiplier (no sum on i). The necessary conditions for a local minimum are given by

$$\frac{\partial L_A}{\partial \xi^k} = 0\,, \quad k = 1,\ldots,N_{\mathrm{i.p.}}\,. \tag{45}$$

Substituting Equation (44) in Equation (45) results in

$$2\left(\xi^k - \psi_{;i}^a(\mathbf{X}^k) \right) + \lambda_i^a w_k = 0\,, \quad k = 1,\ldots,N_{\mathrm{i.p.}}\,. \tag{46}$$

Let the solution of this set of equations be denoted as d_i^{ak}. The scalar values d_i^{ak} are the modified derivatives for each shape-function derivative, $\psi_{;i}^a(\mathbf{X}^k)$, $a = 1,\ldots,N_v$, in each coordinate direction, $i = 1,2,3$, at each volume quadrature point, $\mathbf{X}^k$, $k = 1,\ldots,N_{\mathrm{i.p.}}$, within the element. Additionally, setting to zero the partial derivative of L_A, with respect to the Lagrange multiplier, recovers the integration-consistency constraint

$$\sum_{k=1}^{N_{\mathrm{i.p.}}} w_k\, d_i^{ak} - \sum_{l=1}^{N_{\mathrm{i.p.}}^{\Gamma}} w_l^{\Gamma}\, \psi^a(\mathbf{X}^l)\, n_i^l = 0\,. \tag{47}$$

The proof of the identity Equation (42) is given first. Summing Equation (46) from $a = 1$ to $a = N_v$ results in

$$2 \left[\sum_{a=1}^{N_v} d_i^{ak} - \sum_{a=1}^{N_v} \psi_{;i}^a(\mathbf{X}^k) \right] + w_k \sum_{a=1}^{N_v} \lambda_i^a = 0 . \tag{48}$$

Differentiating the partition of unity relation, Equation (36), in each coordinate direction gives $\sum_{a=1}^{N_v} \psi_{;i}^a(\mathbf{X}) = 0$, $\mathbf{X} \in \Omega_e$ so that the second term in the brackets in Equation (48) is identically zero, resulting in

$$2 \sum_{a=1}^{N_v} d_i^{ak} + w_k \sum_{a=1}^{N_v} \lambda_i^a = 0 . \tag{49}$$

Multiplying Equation (49) by w_k and summing from $k = 1$ to $k = N_{\text{i.p.}}$ gives

$$2 \sum_{k=1}^{N_{\text{i.p.}}} w_k \sum_{a=1}^{N_v} d_i^{ak} + \sum_{k=1}^{N_{\text{i.p.}}} w_k^2 \sum_{a=1}^{N_v} \lambda_i^a = 0 . \tag{50}$$

Summing the integration-consistency constraint, Equation (47), from $a = 1$ to $a = N_v$ results in

$$\sum_{a=1}^{N_v} \sum_{k=1}^{N_{\text{i.p.}}} w_k \, d_i^{ak} - \sum_{a=1}^{N_v} \sum_{l=1}^{N_{\text{i.p.}}^\Gamma} w_l^\Gamma \, \psi^a(\mathbf{X}^l) \, n_i^l = 0 . \tag{51}$$

Rearranging the summations gives

$$\sum_{k=1}^{N_{\text{i.p.}}} w_k \sum_{a=1}^{N_v} d_i^{ak} - \sum_{l=1}^{N_{\text{i.p.}}^\Gamma} w_l^\Gamma n_i^l \sum_{a=1}^{N_v} \psi^a(\mathbf{X}^l) = 0 . \tag{52}$$

From the partition of unity relation, Equation (36), the second summation in the second term in Equation (52) is identically one, resulting in

$$\sum_{k=1}^{N_{\text{i.p.}}} w_k \sum_{a=1}^{N_v} d_i^{ak} - \sum_{l=1}^{N_{\text{i.p.}}^\Gamma} w_l^\Gamma n_i^l = 0 . \tag{53}$$

By assumption, the discrete version of Gauss's theorem, Equation (39), holds so that the second term in Equation (53) is identically zero. Substituting the remaining identity, $\sum_{k=1}^{N_{\text{i.p.}}} w_k \sum_{a=1}^{N_v} d_i^{ak} = 0$, for the first term in Equation (50) results in

$$\sum_{k=1}^{N_{\text{i.p.}}} w_k^2 \sum_{a=1}^{N_v} \lambda_i^a = 0 . \tag{54}$$

The fact that $\sum_{k=1}^{N_{\text{i.p.}}} w_k^2 > 0$ gives the identity $\sum_{a=1}^{N_v} \lambda_i^a = 0$. Substituting this identity into Equation (49) results in $\sum_{a=1}^{N_v} d_i^{ak} = 0$, which is the desired result, Equation (42).

The proof of identity Equation (43) remains. Multiplying Equation (46) by the nodal position vectors, X_j^a, and summing from $a = 1$ to $a = N_v$ gives

$$2 \left[\sum_{a=1}^{N_v} d_i^{ak} X_j^a - \sum_{a=1}^{N_v} \psi_{;i}^a(\mathbf{X}^k) X_j^a \right] + w_k \sum_{a=1}^{N_v} \lambda_i^a X_j^a = 0 . \tag{55}$$

Differentiating the linear consistency relations, Equation (37), in each coordinate direction results in $\sum_{a=1}^{N_v} \psi_{,i}^a(\mathbf{X}) X_j^a = \delta_{ij}$, $\mathbf{X} \in \Omega_e$. Substituting this result for the second term in the brackets in Equation (55) gives

$$2\left[\sum_{a=1}^{N_v} d_i^{ak} X_j^a - \delta_{ij}\right] + w_k \sum_{a=1}^{N_v} \lambda_i^a X_j^a = 0 \,. \tag{56}$$

Multiplying Equation (56) by w_k and summing from $k = 1$ to $k = N_{\text{i.p.}}$ result in

$$2\left[\sum_{k=1}^{N_{\text{i.p.}}} w_k \sum_{a=1}^{N_v} d_i^{ak} X_j^a - \delta_{ij} \sum_{k=1}^{N_{\text{i.p.}}} w_k\right] + \sum_{k=1}^{N_{\text{i.p.}}} w_k^2 \sum_{a=1}^{N_v} \lambda_i^a X_j^a = 0 \,. \tag{57}$$

From Equation (38), the sum in the second term in the brackets in Equation (57) is identically V, so that

$$2\left[\sum_{k=1}^{N_{\text{i.p.}}} w_k \sum_{a=1}^{N_v} d_i^{ak} X_j^a - \delta_{ij} V\right] + \sum_{k=1}^{N_{\text{i.p.}}} w_k^2 \sum_{a=1}^{N_v} \lambda_i^a X_j^a = 0 \,. \tag{58}$$

Multiplying the integration-consistency constraint, Equation (47), by the nodal position vectors, X_j^a, and summing from $a = 1$ to $a = N_v$ give

$$\sum_{a=1}^{N_v} X_j^a \sum_{k=1}^{N_{\text{i.p.}}} w_k d_i^{ak} - \sum_{a=1}^{N_v} X_j^a \sum_{l=1}^{N_{\text{i.p.}}^\Gamma} w_l^\Gamma \psi^a(\mathbf{X}^l) n_i^l = 0 \,. \tag{59}$$

Rearranging the summations gives

$$\sum_{k=1}^{N_{\text{i.p.}}} w_k \sum_{a=1}^{N_v} d_i^{ak} X_j^a - \sum_{l=1}^{N_{\text{i.p.}}^\Gamma} w_l^\Gamma n_i^l \sum_{a=1}^{N_v} \psi^a(\mathbf{X}^l) X_j^a = 0 \,. \tag{60}$$

From the linear consistency relation, Equation (37), the second summation in the second term in Equation (60) is identically X_j^l, resulting in

$$\sum_{k=1}^{N_{\text{i.p.}}} w_k \sum_{a=1}^{N_v} d_i^{ak} X_j^a - \sum_{l=1}^{N_{\text{i.p.}}^\Gamma} w_l^\Gamma n_i^l X_j^l = 0 \,. \tag{61}$$

By assumption, the discrete version of Gauss's theorem is valid, Equation (40), so that the second term in Equation (61) is identically $V\delta_{ij}$. Equation (61) reduces to

$$\sum_{k=1}^{N_{\text{i.p.}}} w_k \sum_{a=1}^{N_v} d_i^{ak} X_j^a = V\delta_{ij} \,. \tag{62}$$

Substituting this expression for the first term in the brackets in Equation (58) results in the bracket term vanishing. The remaining term gives the identity

$$\sum_{k=1}^{N_{\text{i.p.}}} w_k^2 \sum_{a=1}^{N_v} \lambda_i^a X_j^a = 0 \,. \tag{63}$$

The fact that $\sum_{k=1}^{N_{\text{i.p.}}} w_k^2 > 0$ results in $\sum_{a=1}^{N_v} \lambda_i^a X_j^a = 0$. Substituting this identity into Equation (56) gives $\sum_{a=1}^{N_v} d_i^{ak} X_j^a = \delta_{ij}$, which is the desired result, Equation (43). $\qquad \square$

Note that Theorem 2 applies to any set of shape functions with the reproducing properties of Equations (36) and (37), not just harmonic shape functions, and to any integration scheme with the first-order properties of Equations (38) through (40). Interestingly, the values of the shape functions at the volume quadrature points are not used in the proof. The assumptions given in Equation (39) and (40) can be satisfied by using a faceted surface with an integration rule on each facet that can integrate a linear function exactly. This requirement can be satisfied by placing a quadrature point at the centroid of each facet with a weight equal to the area of the facet. For the examples presented in this paper, a facet integration rule was adopted that can exactly integrate polynomials through second order. Table IV gives the error in the derivative-consistency properties, Equation (29), of the polyhedral shape functions *after* the derivative-correction process, for the polyhedral element shown in Figure 5, for subdivision levels $r0$, $r1$, and $r2$. Comparison with results given in Table II shows no corruption of the derivative-consistency properties.

Figure 10(b) shows the stress result from the Voronoi patch test using the modified shape-function derivatives. The maximum error in the stress component σ_{11} is now 1.4×10^{-12} compared with 18% previously (exact value is $\sigma_{11} = 1.0$). This result, along with results of the patch test using the hexahedral patch shown in Figure 8(a), is given in Table V. For the hexahedral patch, the stress error is 8.6% before the derivative correction and 8.8×10^{-16} after the derivative correction. For comparison, the stress error in the patch test for the standard trilinear formulation, where no correction is necessary, is also given. The result for the hexahedral patch using both formulations is also given. For this hybrid case, the interior hexahedron uses the polyhedral formulation, and the six hexahedra on the boundary use the trilinear formulation. The stress error after derivative correction is on the order of machine precision indicating that the two formulations are compatible. However, note that the shape functions between the two elements are not continuous, even though the patch test is satisfied. If desired, the polyhedral element formulation presented here could be modified slightly to use the bilinear mapping on quadrilateral faces to ensure continuity between the two element types. This is not explored here. Results from patch tests applying other stress components yielded similar results.

If desired, a mean-quadrature form of the element formulation could be obtained as a special case of the derivative modification procedure, although a stabilization term in the weak form would need to be added to preclude zero energy modes and restore coercivity. For this special case, there would be no need to actually solve for the harmonic shape functions on the interior of the element.

Table IV. Error in the derivative-consistency properties (29) of the polyhedral shape functions *after* the derivative correction process, for the polyhedral element shown in Figure 5, for different levels of the tetrahedral subdivision. Comparison with results from Table II shows no corruption of these consistency properties. Here, d_i^{ak} represents the modified value of the derivative $\psi_{,i}^a$ at the quadrature point $\mathbf{X}^k$.

Subdivision	$\displaystyle\max_{\substack{k \in \{1,\ldots,N_{\text{i.p.}}\} \\ i \in \{1,2,3\}}} \left[\sum_{a=1}^{N_{\text{v}}} d_i^{ak} \right]$	$\displaystyle\max_{\substack{k \in \{1,\ldots,N_{\text{i.p.}}\} \\ i,j \in \{1,2,3\}}} \left[\sum_{a=1}^{N_{\text{v}}} d_i^{ak} X_j^a - \delta_{ij} \right]$
$r0$	1.19×10^{-15}	4.44×10^{-16}
$r1$	2.89×10^{-15}	5.55×10^{-16}
$r2$	8.77×10^{-15}	1.47×10^{-15}

Table V. Maximum error in the stress component σ_{11} for various patch tests (cf. Figure 10), with and without the necessary correction to the shape-function derivatives to satisfy the integration-consistency constraint. The exact value is 1.0. The $r1$–subdivision was used to calculate the shape functions.

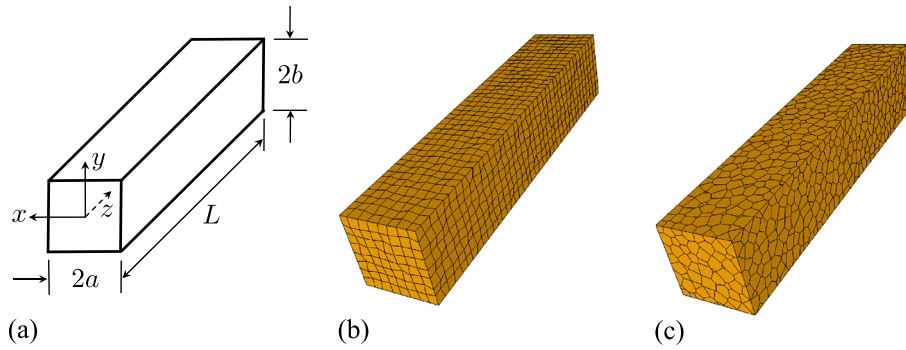| Case	Without derivative correction	With derivative correction
Hex patch, trilinear formulation	1.11×10^{-15}	–
Hex patch, poly formulation	0.0863	5.55×10^{-16}
Hex patch, trilinear and poly	0.0152	8.88×10^{-16}
Random Voronoi patch	0.1844	1.41×10^{-12}

Figure 11. (a) Prismatic beam of length L and rectangular cross-section of width $2a$ and height $2b$. For the presented examples, $L = 5$ and $2a = 2b = 1$. (b) A structured hexahedral mesh with mesh density $8 \times 8 \times 40$. A random perturbation of 20% of the element size was applied to each node while maintaining the exact boundary geometry. (c) Random close-packed Voronoi mesh with a hard-sphere seeding diameter of 0.125.

Instead, Equation (33) would be used to obtain the mean shape-function derivative directly using only the boundary values, with $N_{\text{i.p.}} = 1$ and $w_1 = V$. This special case is analogous to the procedure used by Chen in the development of a stabilized nodally integrated meshless method [18]. Also, Dohrmann and Rashid [35] have developed a higher-order mean-quadrature finite element formulation based on a polynomial approximation of the derivatives of the shape functions. This polynomial approximation uses only the geometry of the element boundaries.

7. EXAMPLES

Consider the prismatic beam shown in Figure 11(a) with length $L = 5$, width $2a = 1$, and height $2b = 1$. The beam is fixed (weakly) on one end, and two loading conditions are considered: (1) bending due to an end-shear load and (2) pure torsion. The special case of linear elasticity is considered. The material is taken to be homogeneous and isotropic with Young's modulus $E = 1.0$ and Poisson's ratio $\nu = 0.3$. Three types of meshes are considered: (1) a structured hexahedral mesh; (2) a structured hexahedral mesh with random perturbations applied to the vertices to create distorted elements; and (3) a random close-packed Voronoi mesh. Example meshes are shown in Figure 11. Five levels of mesh refinement are considered for the structured hexahedral mesh: $N_x \times N_y \times N_z = 2 \times 2 \times 10$, $4 \times 4 \times 20$, $8 \times 8 \times 40$, $16 \times 16 \times 80$, and $32 \times 32 \times 160$. The random perturbations of the nodes are applied in all three coordinate directions for interior vertices. Vertices on the beam face are only perturbed within the face. Similarly, vertices on the beam edges are only perturbed along the edge. The corner vertices are not perturbed. A perturbation of 20% relative to the nominal element size is used. Larger perturbation values were attempted but resulted in a negative Jacobian in the trilinear hexahedral mapping for at least one element. Four levels of mesh refinement are considered for the Voronoi mesh corresponding to a hard-sphere seeding diameter of 0.5, 0.25, 0.125, and 0.0625. The maximum element diameter $D_{\max}$ observed in these Voronoi meshes was approximately 1.0, 0.5, 0.25, and 0.125, respectively. All results for the polyhedral formulation in this section use the $r1$–subdivision to form the harmonic shape functions as described in Section 4.2, except in Figure 18, where the effect of the subdivision level is considered.

The error in the displacement field is measured using the L^2 norm given by

$$\|\mathbf{u}^h - \mathbf{u}\|_2 \doteq \left(\int_\Omega \|\mathbf{u}^h - \mathbf{u}\|^2 \, d\Omega \right)^{1/2},$$ (64)

and the energy semi-norm given by

$$\|\mathbf{u}^h - \mathbf{u}\|_E \doteq \left(\int_\Omega (\boldsymbol{\sigma}^h - \boldsymbol{\sigma}) : (\boldsymbol{\varepsilon}^h - \boldsymbol{\varepsilon}) \, d\Omega \right)^{1/2},$$ (65)

where the superscript h indicates the finite element solution. Here, $\boldsymbol{\sigma}$ is the Cauchy stress tensor, and $\boldsymbol{\varepsilon} = (1/2)(\nabla\mathbf{u} + \nabla\mathbf{u}^{\mathrm{T}})$ is the small strain tensor.

7.1. Bending due to an end-shear load

The exact three-dimensional stress solution for this boundary value problem is given by Barber [36, Ch.17]. This solution is given in Appendix A. A displacement field was derived for use here by integrating the strain field and enforcing compatibility. This displacement field is also given in Appendix A. The exact displacements are prescribed on the face $x = L$. On the face $x = 0$, surface tractions consistent with the exact stress field are prescribed. The four other faces are traction free. Figure 12 shows the Von Mises stress field from the finite element solution of three cases: (1) the hexahedral mesh shown in Figure 11(b) using the trilinear formulation; (2) the same hexahedral mesh but using the polyhedral formulation; and (3) the random close-packed Voronoi mesh shown in Figure 11(c). The two mesh types have roughly the same number of elements, but the Voronoi mesh has roughly four times as many nodes. The stress solutions are qualitatively similar.

The normalized L^2 norm of the displacement error is shown in Figure 13 as a function of mesh refinement for the unperturbed hexahedral mesh. Results for both the trilinear formulation and the polyhedral formulation are given. Figure 13(a) shows results for the mean-dilation formulation, and
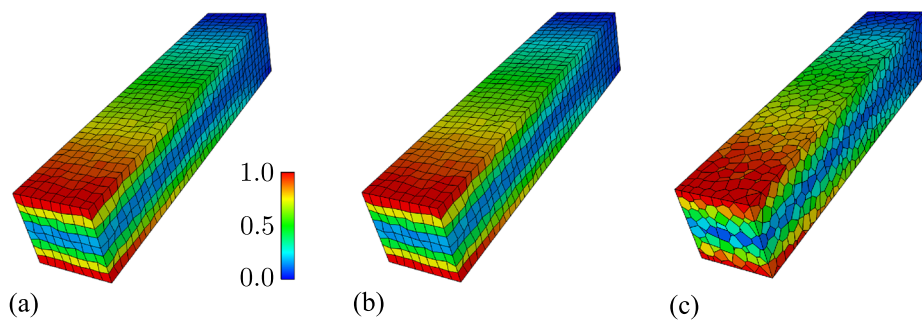
Figure 12. Von Mises stress field from three finite element solutions of the boundary value problem of a cantilever beam subjected to an end-shear load: (a) trilinear hexahedral formulation using the randomly perturbed mesh shown in Figure 11(b); (b) polyhedral formulation using the randomly perturbed mesh shown in Figure 11(b); and (c) polyhedral formulation using the Voronoi mesh shown in Figure 11(c).
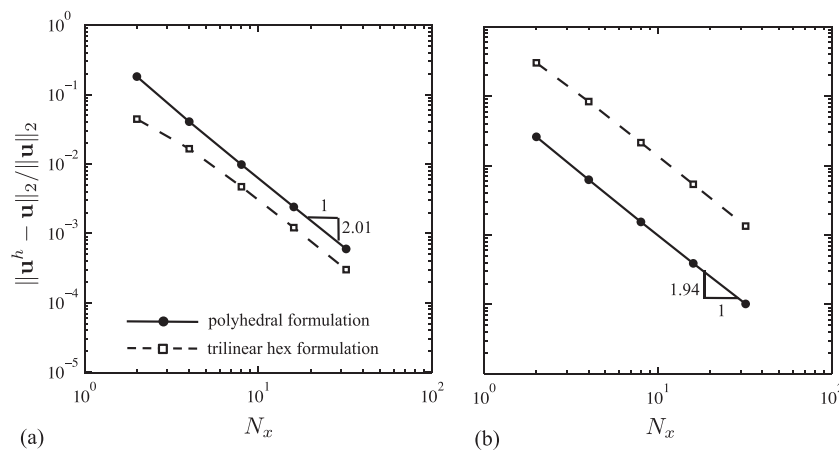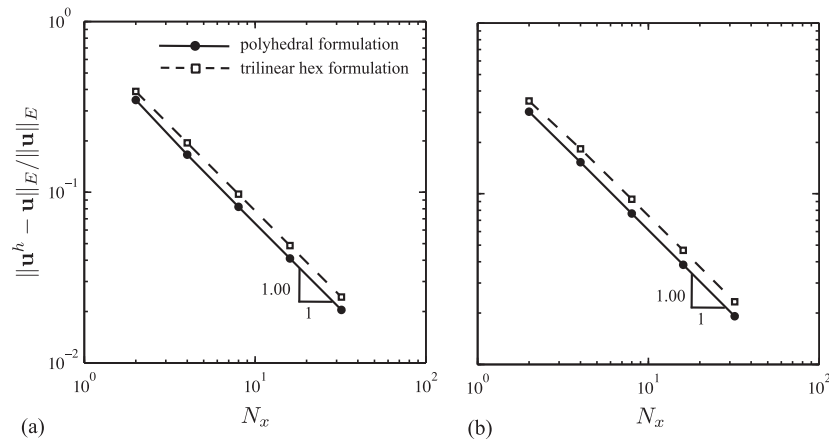

Figure 13. Normalized L^2 norm of the displacement error as a function of mesh density along the beam, N_x, for the boundary value problem of a cantilever beam subjected to an end-shear load, for both the polyhedral formulation and the trilinear hexahedral formulation. (a) mean dilation and (b) standard dilation.

Figure 13(b) shows results for the standard-dilation formulation. At the finest mesh level, the convergence rate is close to the theoretical asymptotic value of 2 for each case. For the same mesh level, the trilinear formulation is more accurate than the polyhedral formulation when the mean-dilation formulation is used. However, the polyhedral formulation is more accurate when the standard-dilation formulation is used. Corresponding results for the energy norm of the displacement error are shown in Figure 14. The convergence rate at the finest mesh level is equal to the theoretical rate of 1. In this norm, the polyhedral formulation is more accurate than the trilinear formulation for both mean-dilation and standard-dilation formulations.

Figure 15 shows the error norms for 20 randomly perturbed hexahedral meshes using the mean-dilation formulation. Each mesh was created using a different random seed. A linear interpolation is shown using the worst-case mesh result. The coarse mesh level $2 \times 2 \times 10$ has the largest variation in

Figure 14. Normalized energy norm of the displacement error as a function of mesh density along the beam, N_x, for the boundary value problem of a cantilever beam subjected to an end-shear load, for both the polyhedral formulation and the trilinear hexahedral formulation. (a) mean dilation and (b) standard dilation.
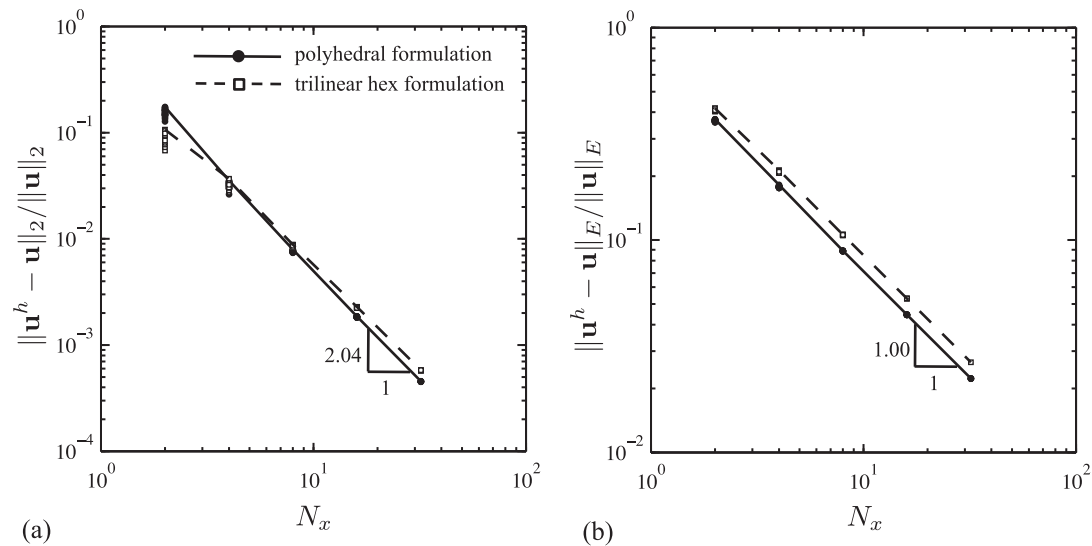
Figure 15. Normalized displacement error as a function of mesh density along the beam, N_x, for the boundary value problem of a cantilever beam subjected to an end-shear load, for both the polyhedral formulation and the trilinear hexahedral formulation, using the randomly perturbed hexahedral mesh and the mean-dilation formulation. Results from 20 simulations (samples) are shown at each mesh resolution. (a) L^2 norm and (b) energy norm.

the L^2 error. There is very little variability in the energy norm. Interestingly, the L^2 error is nearly identical for both the polyhedral formulation and the trilinear formulation, unlike in the unperturbed case (cf. Figure 13). Comparing Figures 13(a) and 15(a), note that the L^2 error of the trilinear formulation is noticeably worse with a distorted hexahedral mesh than an undistorted hexahedral mesh, while the polyhedral formulation shows very little change in the L^2 error. Figure 16 gives results for the random close-packed Voronoi meshes using the mean-dilation formulation. Results for 20 meshes are given at each refinement level. A linear interpolation is drawn using the worst-case mesh result. The coarsest level Voronoi mesh shows much more scatter in the L^2 error norm than did the randomly perturbed hexahedral mesh. The convergence rates at the finest mesh level are given and are close to the theoretical asymptotic values.

To investigate the polyhedral element formulation in the nearly incompressible regime, Figure 17 shows the error norms using the worst-case Voronoi meshes and a mean-dilation formulation for Poisson's ratio values of $\nu = 0.3, 0.4, 0.49, 0.49999$. There is no degradation in convergence rate and absolute accuracy in both the L^2 norm and the energy norm.
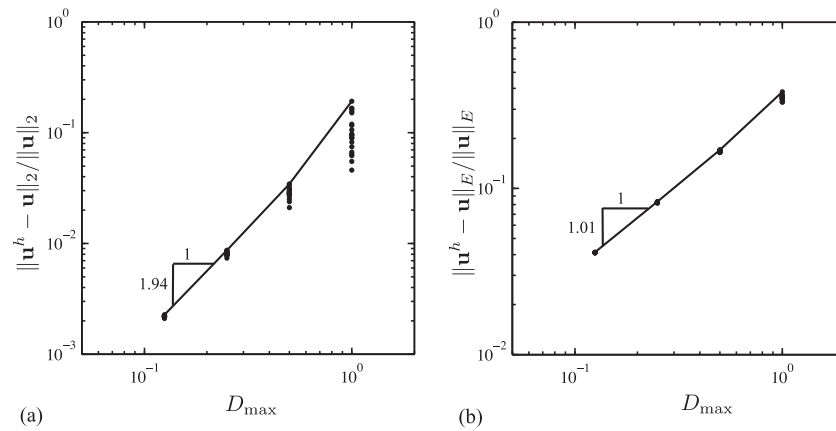
Figure 16. Normalized displacement error as a function of maximum element diameter, $D_{\max}$, for the boundary value problem of a beam subjected to an end-shear load using the random Voronoi mesh and the mean-dilation formulation. Results from 20 simulations (samples) are shown at each mesh resolution. (a) L^2 norm and (b) energy norm.
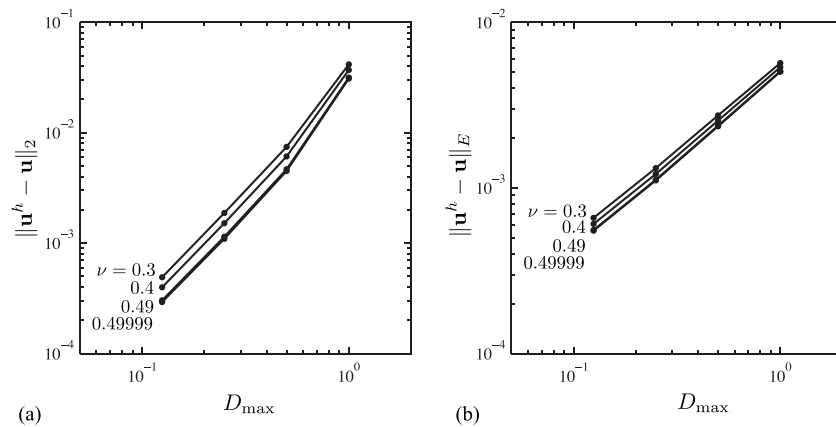
Figure 17. Displacement error as a function of maximum element diameter, $D_{\max}$, for values of Poisson's ratio near the incompressibility limit, for the boundary value problem of a cantilever beam subjected to an end-shear load, using a random close-packed Voronoi mesh and the mean-dilation formulation. The mesh that resulted in the worst case error in Figure 16 at each mesh level is used. (a) L^2 norm and (b) energy norm.

All results for the polyhedral formulation presented up to this point have used the $r1$–subdivision to approximate the harmonic shape functions as described in Section 4.2. Figure 18 compares the error norms using the worst-case Voronoi meshes for subdivisions $r0$, $r1$, and $r2$. Interestingly, for a given mesh resolution, the overall accuracy of the finite element solution does not necessarily increase with a more accurate solution of Equation (14). At least for this boundary value problem, the $r1$–subdivision appears to be optimal. Also, the convergence rate is not affected by the accuracy in the solution for the harmonic shape functions.

7.2. Pure torsion

The exact three-dimensional stress solution for this boundary value problem is given by Barber [36, Ch.16]. This solution is given in Appendix B. A displacement field was derived for use here by integrating the strain field and enforcing compatibility. This displacement field is also given in Appendix B. The exact displacements are prescribed on the face $x = 0$. On the face $x = L$, surface tractions consistent with the exact stress field are prescribed. The four other faces are traction free. Figure 19 shows the Von Mises stress field from the finite element solution of three cases: (1) the hexahedral mesh shown in Figure 11(b) using the trilinear formulation; (2) the same hexahedral mesh but using the polyhedral formulation; and (3) the random close-packed Voronoi mesh shown in Figure 11(c). The two mesh types have roughly the same number of elements, but the Voronoi mesh has roughly four times as many nodes. The stress solutions are qualitatively similar.
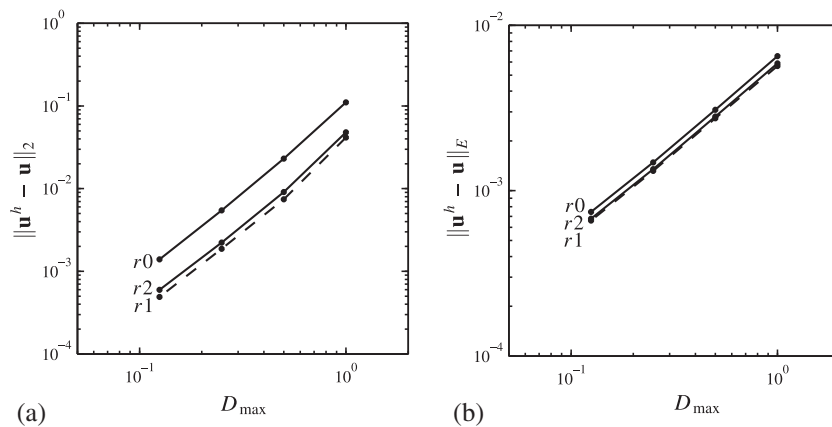
Figure 18. Effect of harmonic shape function accuracy (via the subdivision level $r0$, $r1$, and $r2$) on the displacement error, for the boundary value problem of a beam subjected to an end-shear load, using a random close-packed Voronoi mesh and the mean-dilation formulation. The mesh that resulted in the worst case error in Figure 16 at each mesh level is used. (a) L^2 norm and (b) energy norm.
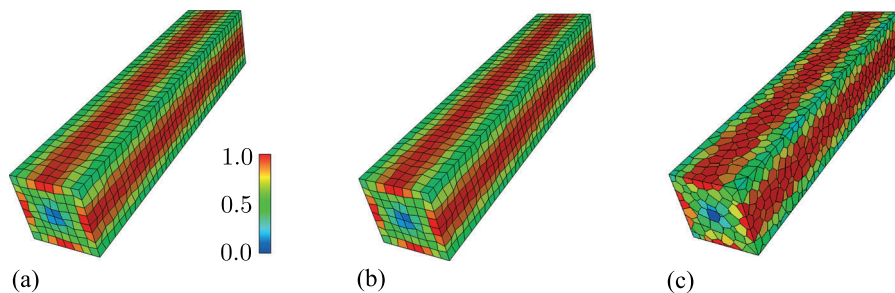

Figure 19. Von Mises stress field from three finite element solutions of the boundary value problem of a beam in pure torsion: (a) trilinear hexahedral formulation using the randomly perturbed mesh shown in Figure 11(b); (b) polyhedral formulation using the randomly perturbed mesh shown in Figure 11(b); and (c) polyhedral formulation using the Voronoi mesh shown in Figure 11(c).

The L^2 norm and energy norm of the displacement error are shown in Figure 20 as a function of mesh refinement for an unperturbed hexahedral mesh. Results for both the trilinear formulation and the polyhedral formulation are given using the mean-dilation formulation. At the finest mesh level, the convergence rate of the L^2 norm of the displacement error is close to the theoretical asymptotic value of 2 for each case. Similarly, the convergence rate of the energy norm of the displacement error is close to the theoretical asymptotic value of 1. For the same mesh level, the polyhedral formulation is more accurate than the trilinear formulation. Recall the bending example, Figure 13(a), in which the trilinear formulation was more accurate for an unperturbed hexahedral mesh.

Figure 21 shows the error norms for 20 randomly perturbed hexahedral meshes using the mean-dilation formulation. Each mesh was created using a different random seed. A linear interpolation is shown using the worst-case mesh result. There is very little variability in both the L^2 norm and the energy norm of the displacement error at any mesh refinement level. Unlike in the bending example, there is very little difference in the norms between the perturbed and the unperturbed hexahedral meshes (cf. Figure 20). Figure 22 gives the results for the random close-packed Voronoi meshes using the mean-dilation formulation. Results for 20 meshes are given at each refinement level. A linear interpolation is drawn using the worst-case mesh result. There is more scatter in the error
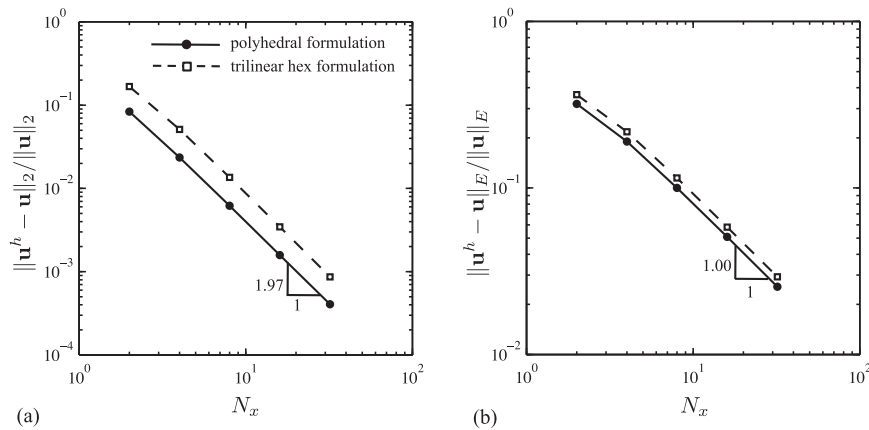
Figure 20. Normalized displacement error as a function of mesh density along the beam, N_x, for the boundary value problem of a beam in pure torsion, for both the polyhedral formulation and the trilinear hexahedral formulation, using the mean dilation formulation. (a) L^2 norm and (b) energy norm.
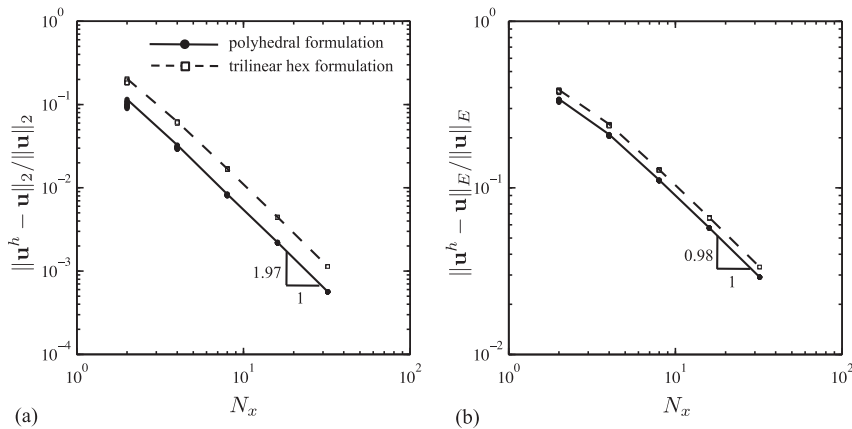

Figure 21. Normalized displacement error as a function of mesh density along the beam, N_x, for the boundary value problem of a beam in pure torsion, for both the polyhedral formulation and the trilinear hexahedral formulation, using the randomly perturbed hexahedral meshes and the mean-dilation formulation. Results from 20 simulations (samples) are shown at each mesh resolution. (a) L^2 norm and (b) energy norm.
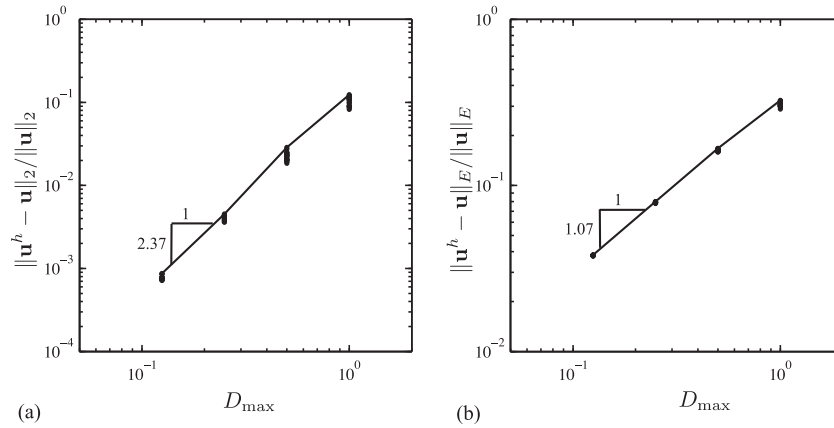
Figure 22. Normalized displacement error as a function of maximum element diameter, $D_{\max}$, for the boundary value problem of a beam in pure torsion, using random close-packed Voronoi meshes and the mean-dilation formulation. Results from 20 simulations (samples) are shown at each mesh resolution. (a) L^2 norm and (b) energy norm.

norms compared with the randomly perturbed hexahedral meshes (cf. Figure 21), but less than the results for the bending examples using the random Voronoi meshes (cf. Figure 16).

7.3. Note on computational cost

In nonlinear solid mechanics, the primary costs of a finite element simulation are in the solution of the discrete system of equations and in the evaluation of the constitutive model at the quadrature points. For explicit time integrators, the primary expense is in the evaluation of the constitutive model. This cost scales with the number of quadrature points in the element. Thus, for the present element formulation, a polyhedral element with 20 nodes, would be 2.5 times more expensive than an eight-node hexahedral element with eight quadrature points. However, an eight-node hexahedral element with eight quadrature points formulated as a polyhedral element would have a comparable cost to the standard trilinear formulation. Additional costs are entailed in the use of a total-Lagrangian formulation for hypoelastic material models. A transformation is required from deformation gradient to rate of deformation and from Cauchy stress to first Piola–Kirchhoff stress. For implicit time integrators, these additional costs are typically dwarfed by the expense of solving the discrete system of equations.

As described in Section 4.2, the construction of the polyhedral shape functions requires an approximate solution of a PDE. The $r0$–approximation involves only one unknown. The $r1$–approximation involves $N_v + N_f + 1$ unknowns. The $r2$–approximation and beyond become increasingly expensive. As indicated in Figure 18, there is no observable benefit from an increased accuracy in the solution of the harmonic shape functions beyond the $r1$–approximation, at least for the presented examples. In any case, because this construction is only performed once, at the beginning of a simulation, its cost is still relatively minor. If desired, the constructed shape function values and their derivatives at the quadrature points could be stored for use in future analyses.

In industrial practice, many times the primary cost of a simulation is the time and expense in actually obtaining a tailored computable mesh of a geometrically complex part. The development of effective polyhedral finite element formulations could significantly reduce this meshing cost.

8. CONCLUSIONS

A displacement-based finite element formulation for general polyhedra was presented for applications in solid mechanics. The polyhedra presented in this paper can have an arbitrary number of vertices or faces. The faces of the polyhedra can have an arbitrary number of edges and can

be nonplanar. The polyhedra can be nonconvex with only the mild restriction of star convexity with respect to the vertex-averaged centroid. Conforming shape functions were constructed using harmonic functions. The shape functions exhibit the Kronecker-delta property at the nodes of the element, thus facilitating the imposition of displacement boundary conditions. An integration scheme was adopted in which the number of quadrature points is equal to the number of vertices. In order to pass the patch test, the shape-function derivatives were modified slightly in order to satisfy a necessary integration-consistency constraint. Surprisingly, this derivative modification did not violate the linear consistency properties of the shape-function derivatives. A proof of this result was given. A mean-dilation formulation was adopted to avoid locking in the nearly incompressible regime. For large deformation analyses, a total-Lagrangian formulation is required because the shape functions and their derivatives are formed in the original configuration.

The patch test was used to demonstrate that the polyhedral formulation of a hexahedron can be used in the same mesh as the trilinear hexahedral formulation, even though their shape functions are not continuous at shared faces. This result enables the use of hybrid poly-hex meshes. If desired, the presented polyhedral formulation could be modified so that quadrilateral faces use the bilinear face mapping of the trilinear hexahedral formulation.

In addition to patch tests, two three-dimensional verification examples were presented using a prismatic beam with a square cross-section: (1) the beam cantilevered and subjected to an end-shear load and (2) the beam subjected to pure torsion. Convergence rates for both the L^2 norm and the energy norm of the displacement error were presented for both random close-packed Voronoi meshes and structured hexahedral meshes. Results were also presented for a randomly perturbed, and thus distorted, hexahedral mesh. For these two examples, the polyhedral formulation performed as good as or better than the conventional trilinear formulation for highly distorted hexahedral meshes.

Although this paper focused on the use of harmonic functions as polyhedral shape functions, other barycentric coordinates could potentially be used as well [37]. The assumption of star convexity could be relaxed to allow for more general nonconvex shapes, albeit with a necessarily more complex element subdivision mesh on which to calculate shape functions and identify the quadrature points and weights.

APPENDIX A: ELASTICITY SOLUTION OF A CANTILEVER BEAM SUBJECTED TO AN END-SHEAR LOAD

Consider a prismatic beam of length L and rectangular cross-section of width $2a$ and height $2b$, with coordinate system shown in Figure 11(a). The beam is fixed (weakly) on the end $x_3 = L$ and subjected to a transverse shear force F in the negative x_2-direction at the opposite end $x_3 = 0$. At any cross-section of the beam,

$$\int_{-b}^{b} \int_{-a}^{a} \sigma_{32} \, dx_1 \, dx_2 = F \quad \text{and} \quad \int_{-b}^{b} \int_{-a}^{a} \sigma_{33} x_2 \, dx_1 \, dx_2 = F x_3 \,, \tag{A.1}$$

so that the beam transmits a constant shear force on each cross-section, and the bending moment about the x_1-axis increases linearly from zero at $x_3 = 0$ to FL at $x_3 = L$. The transverse faces are traction free. For an isotropic material, Barber [36, Ch.17] gives the exact Cauchy stress field as

$$\sigma_{11} = \sigma_{21} = \sigma_{22} = 0 \tag{A.2}$$

$$\sigma_{33} = \frac{F}{I} x_2 x_3 \tag{A.3}$$

$$\sigma_{31} = \frac{F}{I} \frac{2a^2}{\pi^2} \frac{\nu}{1+\nu} \sum_{n=1}^{\infty} \frac{(-1)^n}{n^2} \sin(n\pi x_1/a) \frac{\sinh(n\pi x_2/a)}{\cosh(n\pi b/a)} \tag{A.4}$$

$$\sigma_{32} = \frac{F}{I}\frac{b^2 - x_2^2}{2} + \frac{F}{I}\frac{\nu}{1+\nu}\left[\frac{3x_1^2 - a^2}{6} - \frac{2a^2}{\pi^2}\sum_{n=1}^{\infty}\frac{(-1)^n}{n^2}\cos(n\pi x_1/a)\frac{\cosh(n\pi x_2/a)}{\cosh(n\pi b/a)}\right] \quad (A.5)$$

where ν is Poisson's ratio, and $I = 4ab^3/3$ is the second moment of area about the x_1-axis. Using this stress field, the strain field was obtained from Hooke's law. This strain field was then integrated, and the compatibility constraints were enforced to obtain the following displacement field

$$u_1 = -\frac{F\nu}{EI}x_1x_2x_3 \quad (A.6)$$

$$u_2 = \frac{F}{EI}\left[\frac{\nu}{2}\left(x_1^2 - x_2^2\right)x_3 - \frac{1}{6}x_3^3\right] \quad (A.7)$$

$$u_3 = \frac{F}{EI}\left[\frac{1}{2}x_2\left(\nu x_1^2 + x_3^2\right) + \frac{1}{6}\nu x_2^3 + (1+\nu)\left(b^2 x_2 - \frac{1}{3}x_2^3\right) - \frac{1}{3}a^2\nu x_2 \quad (A.8)\right.$$

$$\left. -\frac{4a^3\nu}{\pi^3}\sum_{n=1}^{\infty}\frac{(-1)^n}{n^3}\cos(n\pi x_1/a)\frac{\sinh(n\pi x_2/a)}{\cosh(n\pi b/a)}\right], \quad (A.9)$$

where E is Young's modulus.

For the evaluation of the infinite series, summation was terminated when the ratio of a term to the current sum was less than 10^{-15} in magnitude. To avoid overflow issues when evaluating the hyperbolic functions, the fractions enclosing these functions were first converted to a form that did not involve the evaluation of the exponential function with a large positive argument.

APPENDIX B: ELASTICITY SOLUTION OF A BEAM SUBJECTED TO PURE TORSION

Consider a prismatic beam of length L and rectangular cross-section of width $2a$ and height $2b$ in a state of pure torsion. For an isotropic material, Barber [36, Ch.16] gives the exact Cauchy stress field as

$$\sigma_{11} = \sigma_{22} = \sigma_{33} = \sigma_{21} = 0 \quad (B.1)$$

$$\sigma_{31} = \mu\beta\sum_{n=1}^{\infty}\frac{16a(-1)^n}{\pi^2(2n-1)^2}\cos\left((2n-1)\frac{\pi}{2}\frac{x_1}{a}\right)\frac{\sinh\left((2n-1)\frac{\pi}{2}\frac{x_2}{a}\right)}{\cosh\left((2n-1)\frac{\pi}{2}\frac{b}{a}\right)} \quad (B.2)$$

$$\sigma_{32} = \mu\beta\left[2x_1 + \sum_{n=1}^{\infty}\frac{16a(-1)^n}{\pi^2(2n-1)^2}\sin\left((2n-1)\frac{\pi}{2}\frac{x_1}{a}\right)\frac{\cosh\left((2n-1)\frac{\pi}{2}\frac{x_2}{a}\right)}{\cosh\left((2n-1)\frac{\pi}{2}\frac{b}{a}\right)}\right] \quad (B.3)$$

where μ is the shear modulus and β is a constant proportional to the total torque applied to the beam. Using this stress field, the strain field was obtained from Hooke's law. This strain field was then integrated, and the compatibility constraints were enforced to obtain the following displacement field

$$u_1 = -\beta x_2x_3 \quad (B.4)$$

$$u_2 = \beta x_1x_3 \quad (B.5)$$

$$u_3 = \beta\left[x_1x_2 + \sum_{n=1}^{\infty}\frac{32a^2(-1)^n}{\pi^3(2n-1)^3}\sin\left((2n-1)\frac{\pi}{2}\frac{x_1}{a}\right)\frac{\sinh\left((2n-1)\frac{\pi}{2}\frac{x_2}{a}\right)}{\cosh\left((2n-1)\frac{\pi}{2}\frac{b}{a}\right)}\right]. \quad (B.6)$$

ACKNOWLEDGEMENTS

REFERENCES

1. Rashid M, Selimotic M. A three-dimensional finite element method with arbitrary polyhedral elements. *International Journal for Numerical Methods in Engineering* 2006; **67**(2):226–252.
2. Ingram D, Causon D, Mingham C. Developments in Cartesian cut cell methods. *Mathematics and Computers in Simulation* 2003; **61**:561–572.
3. Bishop J. Simulating the pervasive fracture of materials and structures using randomly close packed Voronoi tessellations. *Computational Mechanics* 2009; **44**(4):455–471.
4. Bishop J, Martinez M, Newell P. A finite-element method for modeling fluid-pressure induced discrete-fracture propagation using random meshes. *46th US Rock Mechanics / Geomechanics Symposium*, American Rock Mechanics Association: Chicago, IL, USA, 2012; ARMA 12–190.
5. Idelsohn S, Onate E, Calvo N, Pin F. The meshless finite element method. *International Journal for Numerical Methods in Engineering* 2003; **58**(6):893–912.
6. Wicke M, Botsch M, Gross M. A finite element method on convex polyhedra. *Computer Graphics Forum* 2007; **26**(3):355–364.
7. Martin S, Kaufmann P, Botsch M, Wicke M, Gross M. Polyhedral finite elements using harmonic basis functions. *Computer Graphics Forum* 2008; **27**(5):1521–1529.
8. Milbradt P, Pick T. Polytope finite elements. *International Journal for Numerical Methods in Engineering* 2008; **73**(12):1811–1835.
9. Wachspress E. *A Rational Finite Element Basis*. Academic Press: New York, 1975.
10. Warren J. Barycentric coordinates for convex polytopes. *Advances in Computational Mathematics* 1996; **6**:97–108.
11. Hormann K, Sukumar N. Maximum entropy coordinates for arbitrary polytopes. *Computer Graphics Forum* 2008; **27**(5):1513–1520.
12. Jinyun Y. Symmetric Gaussian quadrature formulae for tetrahedronal regions. *Computer Methods in Applied Mechanics and Engineering* 1984; **43**:349–353.
13. Ghosh S. *The Voronoi Cell Finite Element Method*. CRC Press: New York, 2011.
14. Rashid M, Sadri A. The partitioned element method in computational solid mechanics. *Computer Methods in Applied Mechanics and Engineering* 2012; **237–240**:152–165.
15. Joshi P, Meyer M, DeRose T, Green B, Sanocki T. Harmonic coordinates for character articulation. *ACM Transactions on Graphics* 2007; **26**(3):Article 71.
16. Belytschko T, Liu W, Moran B. *Nonlinear Finite Elements for Continua and Structures*. Wiley: London, 2000.
17. Krongauz Y, Belytschko T. Consistent pseudo-derivatives in meshless methods. *Computer Methods in Applied Mechanics and Engineering* 1997; **146**(2–3):371–386.
18. Chen J, Wu C, Yoon S, You Y. A stabilized conforming nodal integration for Galerkin mesh-free methods. *International Journal for Numerical Methods in Engineering* 2001; **50**:435–466.
19. Dohrmann C, Key S. A transition element for uniform strain hexahedral and tetrahedral finite elements. *International Journal for Numerical Methods in Engineering* 1999; **44**:1933–1950.
20. Key S. Mean and linear quadrature for polyhedral finite elements. *Technical Report*, Sandia National Laboratories, (in preparation).
21. Brezzi F, Lipnikov K, Simoncini V. A family of mimetic finite difference methods on polygonal and polyhedral meshes. *Mathematical Models and Methods in Applied Sciences* 2005; **15**:1533–1553.
22. Brezzi F, Lipnikov K, Shashkov M, Simoncini V. A new discretization methodology for diffusion problems on generalized polyhedral meshes. *Computer Methods in Applied Mechanics and Engineering* 2007; **196**(37–40):3682–3692.

23. Beirao da Veiga L. A mimetic discretization method for linear elasticity. *ESAIM. Mathematical Modeling and Numerical Analysis* 2010; **44**(2):231–250.
24. Beirao da Veiga L, Brezzi F, Marini L. Virtual elements for linear elasticity problems. *SIAM Journal on Numerical Analysis* 2013; **51**(2):794–812.
25. Beirao da Veiga L, Brezzi F, Cangiani A, Manzini G, Marini L, Russo A. Basic principles of virtual element methods. *Mathematical Models and Methods in Applied Sciences* 2013; **23**(1):199–214.
26. Botsch M, Kobbelt L, Pauly M, Alliez P, Levy B. *Polygon Mesh Processing*. A K Peters, Ltd.: Natick, Massachusetts, 2010.
27. Hughes T. *The Finite Element Method: Linear Static and Dynamic Finite Element Analysis*. Dover: New York, 2000.
28. Strang G, Fix G. *An Analysis of the Finite Element Method*, (2nd edn). Wellesley-Cambridge Press: Wellesley, Massachusetts, 2008.
29. Hackbusch W. *Elliptic Differential Equations: Theory and Numerical Treatment*. Springer-Verlag: Berlin, 1992. Ch. 2.3.
30. Mousavi S, Sukumar N. Numerical integration of polynomials and discontinuous functions on irregular convex polygons and polyhedrons. *Computational Mechanics* 2011; **47**(5):535–554.
31. Davis P. *Interpolation and Approximation*. Blaisdell Publishing Company: New York, 1963.
32. Cowper G. Gaussian quadrature formulas for triangles. *International Journal for Numerical Methods in Engineering* 1973; **7**(3):405–408.
33. Simo J, Hughes T. *Computational Inelasticity*. Springer: New York, 1998.
34. Luenberger D. *Linear and Nonlinear Programming*, (2nd edn). Kluwer Academic Publishers: Boston, 2003.
35. Dohrmann C, Rashid M. Polynomial approximation of shape function gradients from element geometries. *International Journal for Numerical Methods in Engineering* 2002; **53**(4):945–958.
36. Barber J. *Elasticity*. Springer: New York, 2010.
37. NSF workshop on barycentric coordinates in geometry processing and finite/boundary element methods, July 25–27, 2012. (Available from: http://www.inf.usi.ch/hormann/nsfworkshop/index.html) [accessed on 19 December 2012].